The Journal of the Astronautical Sciences manuscript No.
(will be inserted by the editor)

Mode Analysis for Long-Term Behavior in a Resonant Earth–Moon Trajectory*

Cody Short · Kathleen Howell
Amanda Haapala · Donald Dichmann

Received: 22 April 2016 / Accepted: 13 September 2016

Abstract Trajectory design in chaotic regimes allows for the exploitation of system dynamics to achieve certain behaviors. For example, for the Transiting Exoplanet Survey Satellite (TESS) mission, the selected science orbit represents a stable option well-suited to meet the mission objectives. Extended analysis of particular solutions nearby in the phase space reveals transitions into desirable terminal modes induced by natural dynamics. This investigation explores the trajectory behavior and borrows from flow-based analysis strategies to characterize modes of such a motion. Perturbed initial states from a TESS-like orbit are evolved to supply motion suitable for contingency analysis. Through the associated analysis, mechanisms are identified that drive the spacecraft into particular modes and supply conditions necessary for such transitions.

Keywords Multi-body dynamical systems · Ephemeris trajectory analysis Cauchy–Green strain tensor · Finite-time Lyapunov exponent · Frequency analysis · Numerical perturbations

* This is the authors' accepted manuscript. The final publication is available at Springer via http://dx.doi.org/10.1007/s40295-016-0098-9

C. Short · K. Howell · A. Haapala
School of Aeronautics and Astronautics, Purdue University, 701 West Stadium Avenue, West Lafayette, IN 47907.
E-mail: crshort@purdue.edu

C. Short
Present address: Analytical Graphics, Inc., 220 Valley Creek Boulevard, Exton, PA 19341.

A. Haapala
Present address: The Johns Hopkins University Applied Physics Laboratory, 11100 Johns Hopkins Road, Laurel, MD 20723.

D. Dichmann
NASA Goddard Space Flight Center, 8800 Greenbelt Road, Greenbelt, MD, 20771.

1 Introduction

Trajectory design in chaotic regimes where complex motion is imparted from various gravitational sources allows for the exploitation of the natural dynamics to achieve desirable orbital behaviors. In the case of the Transiting Exoplanet Survey Satellite (TESS) mission, the science orbit is designed as a 2:1 resonant orbit with respect to the lunar orbital period in the Earth–Moon system (Dichmann et al. 2014). A particular solution resembling the TESS science orbit reflects this resonance configuration and is depicted in both the Earth Mean Equatorial J2000 and the Earth–Moon rotating frames in Figure 1. Ten periods of the spacecraft path (throughout five sidereal lunar cycles) are illustrated, and the associated evolution is indicated by color, ranging from blue to red through a traditional spectrum color mapping. During the nominal 2–4 year mission, the spacecraft will observe distant stars with the goal of identifying extrasolar planets, and the selected science orbit represents a stable option that is well-suited to meet the mission objectives.

Long-term analysis of particular solutions that are nearby the TESS science orbit in phase space, reveals transitions into desirable terminal modes induced by the natural dynamics. This investigation explores various components of the trajectory behavior and borrows from flow-based strategies (Anderson et al. 2003; Harden et al. 2014; Short and Howell 2014; Short et al. 2015) to characterize modes of the trajectory. The ultimate goal is the identification and characterization of the mechanism that drives the spacecraft into a particular mode as well as the conditions necessary for such a transition.

The dynamical regime corresponding to the TESS mission trajectory presents many complex and chaotic interactions. While the science orbit associated with the TESS spacecraft has been numerically demonstrated to be operationally stable (Dichmann et al. 2014), higher-fidelity effects allow for the possibility of unpredictable behavior over longer time intervals. Such a situation is well-suited to analysis of force component contributions for the purpose of potentially fabricating transitions into desirable modes. Well-known analysis strategies for investigating trajectory behavior are augmented by computations of Cauchy–Green eigenmetrics. A combination of approaches may enable exploitation of the natural dynamics to accomplish mission objectives.

While this paper explores a specific example case, that of the TESS science orbit, various aspects of the general methodology represent the primary contribution of the work. An overview of the high-level strategy helps to establish context:

1. An initial region of phase space, centered on a state of interest, is selected.
2. The phase-space region is allowed to evolve under the dynamical flow.
3. Traditional analysis methods augmented with flow-based strategies are implemented to identify salient behaviors.
4. Chaotic transitions are noted, and potential triggers are identified if possible.
5. Transitions are artificially induced by emulation at desirable times, subject to specific mission constraints.

This strategy may be applied generically and, in this case, finds an effective illustration in the TESS mission.

Relevant notions related to orbital resonance in general, as well as the particular resonance associated with the TESS mission orbit, serve as a basis for the investigation. Fundamentals of flow-based strategies and a summary of the dy-

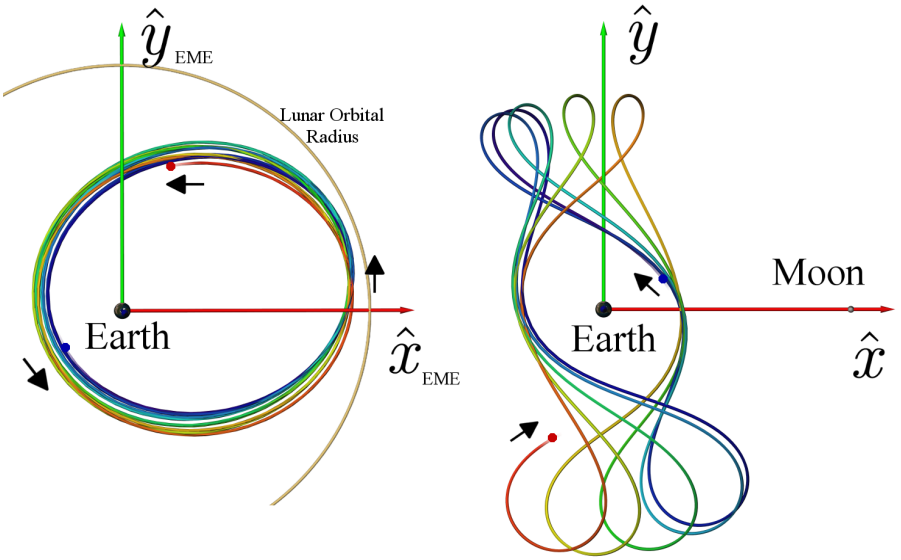

(a) Earth Mean Equatorial of J2000 View (b) Earth–Moon Rotating Frame View

Fig. 1 10 Periods of a TESS-like Science Orbit Computed in an Ephemeris Model

namical system models are also offered; some material follows directly from Short and Howell (2014) as well as Short et al. (2015). Several strategies for increasing the understanding of the long-term behavior of the TESS science orbit are highlighted in the analysis. These strategies include a discussion of perturbation theory, particularly with respect to the Kozai parameter, and inspection of model components. The examination of orbital elements and frequency components over time supplies some additional insight. A flow-based approach lends context to particular solutions and the effects of perturbations on these solutions. Finally, conditions for achieving particular results that display desirable behavior modes are offered prior to a few concluding remarks.

2 Background

2.1 Resonant orbits and TESS

Many interesting natural solar system behaviors can only be understood within the context of resonances that exist between the motions of the associated bodies. Recently, efforts to exploit resonance for spacecraft trajectory design have become a focus for practical applications. In particular, researchers have explored the possibility of harnessing resonant orbits for transfer trajectories (Parker and Lo 2004; Anderson and Lo 1996; Vaquero and Howell 2014), and for stable orbits with desirable repeating motions (Carrico et al. 2011; Dichmann et al. 2014, 2015). Such strategies support useful mission options, and reflect the potential afforded by carefully navigating a chaotic design space.

Of particular relevance for spacecraft trajectories are orbit-orbit resonances. Such resonances are those where the spacecraft's motion repeats in a near-integer ratio relationship with the motion of a massive system body. For example, in the Earth–Moon system, the Moon orbits the Earth once every sidereal period, q, of $\sim$27.3 days. A spacecraft moving in the Earth–Moon system with a characteristic period, p, that is some multiple of the Moon's period is said to be moving in a p:q resonance with the Moon. If the spacecraft completes two revolutions for each revolution of the Moon, this resonance is designated as a 2:1 resonance. Such exact integer ratio behaviors only appear in simple models of the dynamical system behavior. However, within higher-fidelity-model contexts, motion that oscillates about such resonances frequently persists and is often reflective of stable behavior.

The Transiting Exoplanet Survey Satellite (TESS) mission orbit is selected in a nearly 2:1 resonance with the Moon in the Earth–Moon system. Thus, the orbit is characteristic of a period roughly half that of the lunar sidereal period, or $\sim$13.67 days. The TESS mission uses a lunar flyby to reach its science orbit (Dichmann et al. 2014). The lunar flyby is required to raise perigee to 17 Earth radii (r_e), and to raise inclination. The post-flyby apogee radius, approximately 80 r_e, is chosen to achieve the desired phasing: When the spacecraft reaches perigee after flyby, the spacecraft is nearly aligned with the Moon. In practice a misalignment as high as 35^o is acceptable. At the post-flyby perigee, a Period Adjust Maneuver (PAM) is performed to lower apogee to 59 r_e thereby achieving the resonance orbit period of 13.67 days. When the spacecraft reaches apogee one-half revolution later, the Moon has traveled a quarter of its orbit, so at spacecraft apogee the spacecraft-Earth-Moon angle is around $90^o \pm 35^o$.

While the orbit does not generally complete exactly two revolutions for each revolution of the Moon, it can be described as "in oscillation" about such a resonance (Dichmann et al. 2014). The orbit resonance implies that at spacecraft apogee the spacecraft-Earth-Moon angle remains around 90^o. This is called the Lunar Resonant Phasing (LRP) condition. The LRP condition prevents close approaches with the Moon and helps to achieve operational stability. It is convenient to observe such motion in a rotating frame fixed on the motion of the Moon about the Earth. Such a representation appears in the right panel of Figure 1.

It is desirable for the spacecraft orbit to be operationally stable, requiring no stationkeeping, upon entering and for the 2–4 year duration of the science phase of the trajectory. Throughout the nominal mission and for, at least, 100 years beyond the end of the mission,[1] the spacecraft trajectory is also required to avoid the geosynchronous orbital band at all times. The trajectory is designed to satisfy this requirement throughout all mission phases and employs a "dispose-in-place" strategy after the end of the mission. However, extended analysis of the trajectory reveals particular modes where the spacecraft behavior can settle into motion consistent with the avoidance of the geosynchronous band. These modes are trajectory phases induced by the natural dynamics but, without a more complete understanding of the dynamical environment, it is not certain that a perturbation or disturbance would not shift the modes into some undesirable behavior.

[1] The original mission requirement to maintain an orbital altitude above GEO for 100 years has since been relaxed to 30 years. This relaxation is due to analysis indicating that the TESS mission orbit behavior is not definitively predictable beyond 30 years. This analysis is discussed in Dichmann et al. (2016), and is supported by the work described in the current paper.

2.2 Flow-based analysis

The Cauchy–Green Strain Tensor (CGST or CG tensor) describes the relative stretching of nearby trajectories over a given time interval. As such, the CGST offers a means for identifying relatively larger or smaller directions of expansion. For example, this relative information can be identified from the eigenvalues and eigenvectors of the tensor, such as the Finite-Time Lyapunov Exponent (FTLE) values that are obtained from the Cauchy–Green eigenvalues. The CGST is computed using the familiar State Transition Matrix (STM), a matrix that describes the impact of initial state variations on the behavior along trajectories over time. This STM can be calculated by directly observing the effects of perturbed trajectories, or by integrating the first-order variational equations relative to the system equations of motion.

The flow map, $\phi_{t_o}^{t}(\boldsymbol{x}_o)$, represents the state of the system that has evolved to a final time t from an initial state $\boldsymbol{x}_o$ at time t_o. The matrix product, $\mathbf{C} = \Phi_{t_o}^{t}(\boldsymbol{x}_o)^{\mathsf{T}}\Phi_{t_o}^{t}(\boldsymbol{x}_o)$, is the Cauchy–Green strain tensor (Smith 1993), and the individual matrix, $\Phi_{t_o}^{t}(\boldsymbol{x}_o) = \frac{d\phi_{t_o}^{t}(\boldsymbol{x}_o)}{d\boldsymbol{x}_o}$, is the STM evaluated along the arc at time t (here, $^{\mathsf{T}}$ indicates the matrix transpose). Since the state transition matrix supplies the evolution of infinitesimal perturbations to an initial variational state of the system, the Cauchy–Green strain tensor represents a natural object that reveals the growth or decay of these perturbations. For example, if several adjacent, initial state vectors are separated by small perturbations and subsequently evolved for a prescribed time, the Jacobian is estimated (here, using two dimensions as an example) as described by Haller (2001) via finite differencing such as,

$$\Phi_{t_o}^{t}(\boldsymbol{x}_o)\Big|_{(i,j)} = \frac{d\phi_{t_o}^{t}(\boldsymbol{x}_o)}{d\boldsymbol{x}_o}\Big|_{(i,j)} = \begin{bmatrix} \frac{x_{i+1,j}(t)-x_{i-1,j}(t)}{x_{i+1,j}(t_o)-x_{i-1,j}(t_o)} & \frac{x_{i,j+1}(t)-x_{i,j-1}(t)}{y_{i,j+1}(t_o)-y_{i,j-1}(t_o)} \\ \frac{y_{i+1,j}(t)-y_{i-1,j}(t)}{x_{i+1,j}(t_o)-x_{i-1,j}(t_o)} & \frac{y_{i,j+1}(t)-y_{i,j-1}(t)}{y_{i,j+1}(t_o)-y_{i,j-1}(t_o)} \end{bmatrix}, \quad (1)$$

where the indices i and j indicate relative initial perturbations in either positive or negative senses away from the x and y state components as appropriate.

Various schemes exist for calculating the Jacobian, including numerical integration of the variational equations, direct calculation from a grid of points, as in Equation (1), or through the use of an auxiliary grid as described by Farazmand and Haller (2012). Direct computation from a grid of points that covers the domain of the simulation allows for the determination of the FTLE in systems where variational equations are not available. Selecting an appropriate grid spacing facilitates the identification of flow features consistent with the order of the grid spacing. A mesh with inadequate resolution may exclude some structures. However, an auxiliary grid that brackets each of the primary grid points increases the accuracy of the resulting Jacobian.

Available from the CGST, the largest finite-time Lyapunov exponent[1], is a common metric that quantifies the relative stretching and stability of nearby phase space states as they evolve over time. The FTLE essentially measures the stretching between adjacent trajectories over a prescribed time interval. Mathematically, the calculation of the FTLE is fairly straightforward—it is the largest normalized

[1] While there are as many FTLE values as dimensions in the phase space, the largest finite-time Lyapunov exponent is denoted *the FTLE* value of interest in this analysis.

eigenvalue of $\sqrt{\Phi_{t_o}^{t}(\boldsymbol{x}_o)^{\mathsf{T}}\Phi_{t_o}^{t}(\boldsymbol{x}_o)}$, i.e., the square root of the Cauchy–Green tensor, $\mathbf{C}$. Thus, the FTLE is evaluated from the expression,

$$\lambda = \frac{1}{|T|} \ln \sigma_n \left(\sqrt{\mathbf{C}} \right), \tag{2}$$

where $\sigma_n()$ is the operation that extracts the largest eigenvalue of the operand. The parameter $T = t - t_o$ is both the truncation time for the computation of the FTLE value and a means of normalizing this value.

Also available from the Cauchy–Green tensor are the directions of extremal stretching in phase space. The evolution of a portion of the phase space over time is related to σ_i and $\boldsymbol{\xi}_i$. Specifically, stretching occurs along the eigenvector, $\boldsymbol{\xi}_i$, proportional to $\sqrt{\sigma_i}$,

$$\left| \mathrm{D}\phi_{t_o}^{t}(\boldsymbol{x}_o)\boldsymbol{\xi}_i \right| = \sqrt{\sigma_i}\, |\boldsymbol{\xi}_i| \,, \tag{3}$$

where $\mathrm{D}\phi$ represents partial differentiation of the flow map ϕ with respect to the state variables—geometrically, the deformation of the phase space induced by the flow. Consequently, the greatest degree of stretching occurs along the eigenvector, $\boldsymbol{\xi}_n$, associated with the largest eigenvalue, σ_n. This notion is illustrated in Figure 2, where the double-headed red arrow represents $\boldsymbol{\xi}_n$ and the double-headed blue

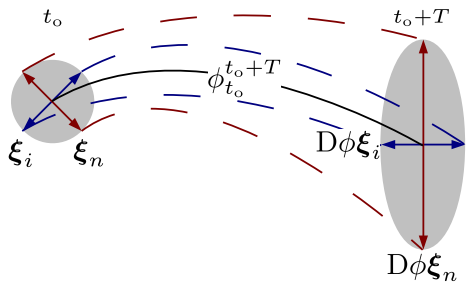

Fig. 2 Stretching Associated with Eigenvectors of the Cauchy–Green Tensor

arrow conveys the remaining directions. As with the largest FTLE value, λ, the eigendirection, $\boldsymbol{\xi}_n$, associated with the largest eigenvalue of $\mathbf{C}$ is also a focus.

Specific analysis strategies are utilized to explore a TESS-like solution. Observation of the orbital characteristics, augmented with predictive FTLE data, indicates when the trajectory is expected to evolve into different modes. The largest finite-time Lyapunov exponent provides a single measure that describes the magnitude of divergence along a path for a given time horizon. Of special interest, for the purposes of this effort, is the model-agnostic nature of the FTLE—such a metric can be calculated for trajectory arcs regardless of the underlying model complexity or characterization. Values for the finite-time Lyapunov exponent may be computed for simplified models and compared with corresponding values from propagations in higher-fidelity models. Moreover, careful selection of the time horizon and the calculation strategy for the FTLE can yield a useful profile that effectively predicts and characterizes general trajectory trends. In this analysis, FTLE profiles supply a signature of conditions that can "trigger" shifts in a particular

solution such that it exhibits various modes of behavior and reveal the transitions between such modes.

Careful inspection of the effects of the model components before, during and after transitions in trajectory behavior raises the possibility for artificially producing such a transition by design. The flow-based FTLE profile suggests a "signature" for trajectory-shifting behavior. Illustrated in Figure 3 is an FTLE profile consistent with a 100-year propagation of the TESS-like orbit. This profile is created by compositing state-transition matrices to form a 1.2-year time horizon for each data point (note where the FTLE profile drops to zero as the time horizon extends beyond the 100-year mark). The time horizon of 1.2 years is selected empirically.

The FTLE profile indicates that the trajectory shifts between different types of behavior modes. Generally, there is some correlation with osculating orbital elements, particularly eccentricity, as larger values of the FTLE are consistent with trajectory behavior exhibiting lower perigee radii (r_p) and higher radii of apogee (r_a), while lower FTLE values indicate trajectory phases with higher r_p and lower r_a. However, the FTLE profile also conveys a measure of relative orbital stability under perturbations as trajectory segments characteristic of low FTLE values also reflect a lower propensity for trajectory divergence. Profiles of FTLE values essentially summarize transitional behavior. Knowledge of qualitative transitions, and

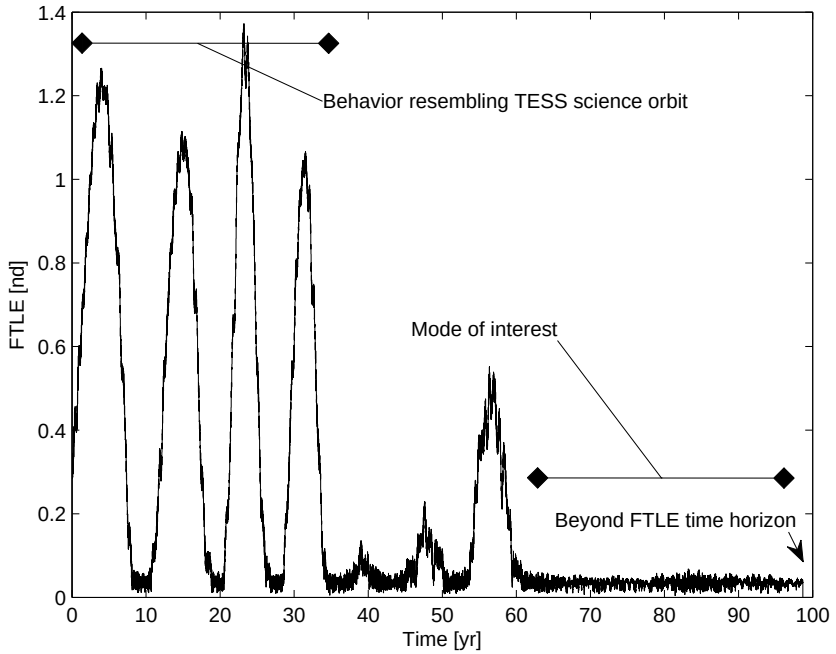

Fig. 3 FTLE Profile for 100-Year TESS-like Science Orbit Propagation

when they might occur, allows for investigation of these behaviors through analysis of the system characteristics. Inspection of the gravitational system geometry and the spacecraft trajectory may yield specific conditions that allow for trajectory shifts into desirable modes. Such an analysis is reflected in this investigation.

2.3 System models

Some key space environments involve multiple significant gravity fields. As such, it is often necessary to incorporate as many of these gravity fields as possible into the governing models to ensure accurate simulation and to capture the essential features of the dynamical interactions. Models directly incorporating more than two gravitating point-mass bodies, however, offer no general analytical solutions, and introduce additional complexities, which may be small but significant. Formulating the problem in terms of three bodies produces a model sufficiently complex to reveal many important characteristics while remaining tractable. However, the general three-body problem possesses no comprehensive, closed-form solution (Diacu 1996). Thus, additional simplifications offer significant insight.

The computation of the CGST is not contingent upon any assumptions in the derivation of the system differential equations, and can be applied to systems modeled with various levels of fidelity. Analysis based on the Cauchy–Green tensor remains valid regardless of the complexity of the model. In this investigation, various levels of model fidelity, including those consistent with the Circular Restricted three-body Problem (CRP), the Elliptic Restricted three-body Problem (ERP), a BiCircular four-body Problem (BCP), and particular EPHemeris formulations (EPH), are all employed. All of these models represent the inclusion of some natural behavior, and comparisons of the behavior consistent with each model can reveal an associated impact on the trajectory evolution. Some considerations for each model are summarized.

2.3.1 The circular restricted three-body model

The circular restricted problem incorporates only the effects of the masses of two larger primaries on a third body of negligible mass, such as a spacecraft. A brief review of the CRP is useful to illustrate the rotating reference frame and summarize the associated equations of motion. The two primary bodies that appear in the model are designated as P_1 and P_2. Position variables, x, y, and z describe the position of the third body, the spacecraft, with respect to the barycenter of the primary system, which also serves as the origin of the rotating and inertial reference frames. The rotating reference frame is defined such that $\hat{x}$ is directed from P_1 to P_2, $\hat{z}$ is perpendicular to the inertial P_2 plane of motion consistent with orbital angular momentum and $\hat{y} = \hat{z} \times \hat{x}$. The system mass parameter is represented by $\mu = \frac{m_2}{m_1+m_2}$, a function of the masses of the primary bodies. Additionally, distances between the third body and the two primaries are denoted r_{i3}. Specifically, in a coordinate frame that rotates coincident with the circular motion of the primaries, a system of differential equations that describes the motion of the third body incorporates the potential function,

$$U^* = \frac{1-\mu}{r_{13}} + \frac{\mu}{r_{23}} + \frac{1}{2}(x^2 + y^2), \tag{4}$$

and is written,

$$\ddot{x} = \frac{\partial U^*}{\partial x} + 2\dot{y}, \quad \ddot{y} = \frac{\partial U^*}{\partial y} - 2\dot{x}, \quad \ddot{z} = \frac{\partial U^*}{\partial z}, \tag{5}$$

where the first derivatives in x and y appear as a result of the Coriolis acceleration.

The equations of motion in the circular restricted problem are consistent with Szebehely (1967) where they admit a single integral of the motion. This integral is termed the Jacobi constant, and is evaluated as,

$$C_{\text{Jacobi}} = 2U^* - v^2, \tag{6}$$

where $v^2 = \dot{x}^2 + \dot{y}^2 + \dot{z}^2$, that is, the square of the magnitude of the relative velocity. This integral allows for a reduction of order in the problem, frequently serves in an important role in the definition of surfaces of section, and establishes boundaries on the physical motion of the third body. These boundaries are defined when $v = 0$ in Equation (6), separating regions of real and imaginary velocities. The circular restricted problem represents a model of sufficient complexity to exhibit regions of both chaotic and ordered behavior. Generally, the focus of analysis in this model is conceptual understanding and the exploitation of any dynamical structures that are associated with the chaotic regions to identify useful trajectory arcs. The CRP model is frequently suitable to yield first-order mission design solutions, but useful information is often difficult to isolate amidst the chaos and small variations to initial states can yield large differences in behavior over time.

2.3.2 The elliptic restricted three-body model

Also described in Szebehely is an extension of the CRP that incorporates elliptic motion of P_2 with respect to P_1. The reference frame becomes a rotating-pulsating frame such that $\hat{x}$ remains directed from P_1 to P_2 while the characteristic distance invoked to nondimensionalize the system variables is equal to, and varies with, P_2's radial distance from P_1 as it evolves on its elliptic path. Such an increment in model fidelity results in a generally nonautonomous system that is time-periodic and may be rendered autonomous if necessary. The independent variable is defined as the true anomaly f along the orbit of P_2 with equivalences to the nondimensional (nd) time-parameter of the CRP at multiples of π. Thus, introducing these modifications to the system differential equations of motion can be accomplished through a change of variables,

$$w = \frac{U^*}{1 + e\cos f}, \tag{7}$$

where e is the orbital eccentricity of the P_2 orbit. Differentiation is performed with respect to f, $()' := \frac{d()}{df}$, and the equations of motion are structurally equivalent to those in the circular restricted problem, i.e.,

$$x'' = \frac{\partial w}{\partial x} + 2y', \quad y'' = \frac{\partial w}{\partial y} - 2x', \quad z'' = \frac{\partial w}{\partial z}. \tag{8}$$

Unlike the CRP, a constant of the motion is not available in the elliptic restricted problem. This slightly more complex model may aid in isolation of the effects of second primary's orbital eccentricity on spacecraft motion.

2.3.3 The bicircular four-body model

A simplified four-body model, similar to the model utilized by Koon et al. (2002) and further explored by Blazevski and Ocampo (2012), is also employed. This model incorporates the influence of a third massive body simultaneously with the dynamical effects of the two primary bodies in the circular restricted problem. The additional massive primary is designated P_4. Although the system is not coherent, the Newtonian inverse-square gravity of P_4 acts on the spacecraft in addition to the gravitational effects of the two CRP primaries. The third primary body does not affect the circular Keplerian orbits of the other primaries. If $\mu_4 = \frac{m_4}{m_1+m_2}$, the equations of motion remain the same as Equations (5), but the potential function is now (Guzman 2001),

$$U^* = \frac{1-\mu}{r_{13}} + \frac{\mu}{r_{23}} + \frac{\mu_4}{r_{43}} + \frac{1}{2}(x^2+y^2). \tag{9}$$

Such a four-body model, while still incorporating significant simplifications, introduces an important transition much like the ERP. The presence of the perturbing fourth body results in a nonautonomous system. As in the elliptic model, the change in the nature of the system decreases the applicability of many of the dynamical systems tools that are available in the CRP, while completely removing others. Again, a constant of the motion, and, consequently, a convenient expression for bounds on the motion, is no longer available. Finally, due to the time-dependent nature of the system, careful consideration is afforded the initial system geometry.

2.3.4 Ephemeris models

Ephemeris models are formulated to be generally consistent with the previous models. Such higher-fidelity systems, similar to the model employed by Pavlak and Howell (2012), are constructed to incorporate position histories for the primary bodies supplied by the JPL developmental ephemerides. The governing equations are derived as the n-body relative equations of motion,

$$\ddot{\boldsymbol{r}}_{ms} = -\frac{\mu_{2b,s}+\mu_{2b,m}}{r_{ms}^3}\boldsymbol{r}_{ms} + \sum_{\substack{j=1 \\ j\neq s,m}}^{n} \mu_{2b,j}\left(\frac{\boldsymbol{r}_{sj}}{r_{sj}^3} - \frac{\boldsymbol{r}_{mj}}{r_{mj}^3}\right). \tag{10}$$

Here, μ_{2b} is the familiar mass parameter from the two-body problem, nondimensionalized as appropriate. The position vector, $\boldsymbol{r}_{mj}$, indicates the position of the j^{th} body with respect to the central body, m; the subscript s is associated with the spacecraft. In this model, states defined in the restricted problem are transitioned to body-centered J2000 states, and vice versa, via an instantaneous rotating frame defined by the ephemeris states.

Such ephemeris models require additional considerations regarding accuracy and computation of the CGST. The accuracy of a particular formulation generally increases as more bodies are included. However, selecting subsets of gravitating bodies allows for comparisons in model-component effects through Cauchy–Green metrics. These models naturally involve six-dimensional state vectors and trajectory propagation proceeds in all spatial dimensions. Computation of the Cauchy–Green tensor employs auxiliary "grid" points about each state variable. Thus, in

this model, one CGST computation involves the propagation of 12 perturbations. Given these higher-dimensional considerations, an effective means for parameterizing a search space is required, and in this case the CG eigenvector $\boldsymbol{\xi}_n$ is utilized.

All of these various models ultimately represent contributions to the natural motions in a system. Different impacts associated with specific motions in two- or three-body gravitational fields are reflected in each model. Despite the varying dynamics, motion observed in each model remains subject to the wide applicability of flow-based analysis. Consequently, comparisons can be made between levels of model fidelity and particular model components may be isolated as triggers for specific behaviors through such comparisons.

3 Analysis

Initial explorations in the phase space nearby the TESS science orbit reveal particular solutions that eventually diverge from the nominal mission orbit but actually exhibit desirable end-of-life behavior. However, the existence of these alternate solutions also implies the potential for undesirable divergence, and a better understanding of the long-term behavior is necessary. Mission requirements constrain the perigee radius for the science phase of the trajectory to remain above 6.7 Earth radii ($\mathrm{r_e}$) to avoid the geosynchronous satellite belt. To minimize communication times for data retrieval, perigee should also remain below 22 $\mathrm{r_e}$ for the duration of the nominal science phase (2–4 years). The TESS mission calls for a dispose-in-place end-of-life strategy where the spacecraft will continue in the mission orbit, and avoidance of the GEO belt continues to be required. However, after the science phase, the upper bound on $\mathrm{r_p}$ is no longer critical. Thus, behavior that settles into an orbit with higher perigee radii has the potential for greater stability while increasing the distance from the geosynchronous satellites.

To identify solutions that evolve into advantageous behavior modes, and to better understand the local neighborhood of perturbations near the reference solution, several strategies are invoked. Initially, a single-parameter exploration of small variations in the rotating-y component of the state at the period adjust maneuver, that is, the maneuver to enter the TESS science orbit, reveals various solutions. Among these solutions are those displaying behavior consistent with the FTLE profile depicted in Figure 3.

Inspection of the long-term behavior of the orbital elements and observation of individual frequency markers supports the characterization of certain behavioral transitions. From a particular solution, investigations in terms of small perturbations reveal additional insight into the long-term trajectory behavior. Toggling model-fidelity and examining the state components aids in illumination of the complexities of the cumulative effects of the various system influences on the spacecraft path over time. Invoking the flow context provides a clear picture of the truly chaotic nature of the system, and supports identification of potentially useful end-of-life solutions. A strategy for identifying specific conditions for entering these solutions is discussed. The chaotic nature of the spacecraft operating environment supplies many possibilities and all of these varied, but ultimately related, analysis options lead to a better general understanding of the system.

3.1 Perturbation theory and the Kozai parameter

Perturbation methods offer useful analysis options for understanding the contributing factors in orbital motion. Colombo (2015) and Colombo et al. (2015) examine the long-term perturbative effects on highly-elliptical and libration point orbits, and explore the possibility of engineering desired end-of-life options for various mission scenarios, including graveyard orbit and re-entry/impact options. The present analysis focuses on understanding the context associated with the effective graveyard orbit represented by the TESS dispose-in-place strategy. Rather than employing analytical or semi-analytical, general perturbation theory, the focus is on special perturbation analysis through numerical simulation.

As a stepping-off point from general perturbations, consider the evolution of the Kozai parameter plotted in Figure 4. This parameter reflects a constant of the motion under the Kozai formulation of the three-body problem where short-term oscillations due to the third-body perturbation are essentially averaged out (Kozai 1962; Lidov 1962; Dichmann et al. 2014). The Kozai parameter is defined,

$$K = \cos i \cdot \sqrt{1 - e^2}, \tag{11}$$

and, similar to the Jacobi constant, is not expected to be conserved in higher-fidelity models. However, its evolution can be observed when calculated instantaneously at each time step along the trajectory using osculating elements. In Equation (11), i is the inclination of the spacecraft orbit with respect to the lunar orbital plane, and e is the orbital eccentricity.

As the Kozai mechanism features heavily in the design strategy for the TESS mission and supports some general trends consistent with the science orbit, (Gangestad et al. 2013; Dichmann et al. 2014) it seems reasonable and appropriate to initiate the present analysis with a discussion of the behavior of the Kozai parameter over time. The TESS orbit in the Design Reference Mission (DRM) has been selected for its transitioning behavior. Thus, the evolution of an initial state slightly perturbed from the TESS DRM trajectory reflects the potential differences in responses. Gangestad et al. (2013) identify a suitable Kozai parameter to be 0.65 to maintain the upper and lower constraints on $\mathrm{r_p}$. Apparent in Figure 4 is an initial value of K that oscillates about values lower than 0.65, and then shifts into two later phases oscillating above 0.65. These differences, aside from being expected as associated with a different solution, illustrate two relevant points. First, much of the previous analysis for the TESS DRM focuses on the first few decades of the mission, and is generally consistent with the results showcased in the orbit selected for this analysis. Second, these behavior-shifting trends, characteristic in many of the orbital measures associated with this solution, are reflective of the different modes through which the trajectory evolves. Various metrics reflect these modes and their associated transitions more or less clearly. This brief inspection of the Kozai parameter serves as an introduction to a series of observations that help establish the perturbed orbit that is investigated in this analysis.

3.2 Orbital elements

Inspection of the evolution of the osculating orbital elements serves to further establish the long-term behavior exhibited by a given particular solution. Given

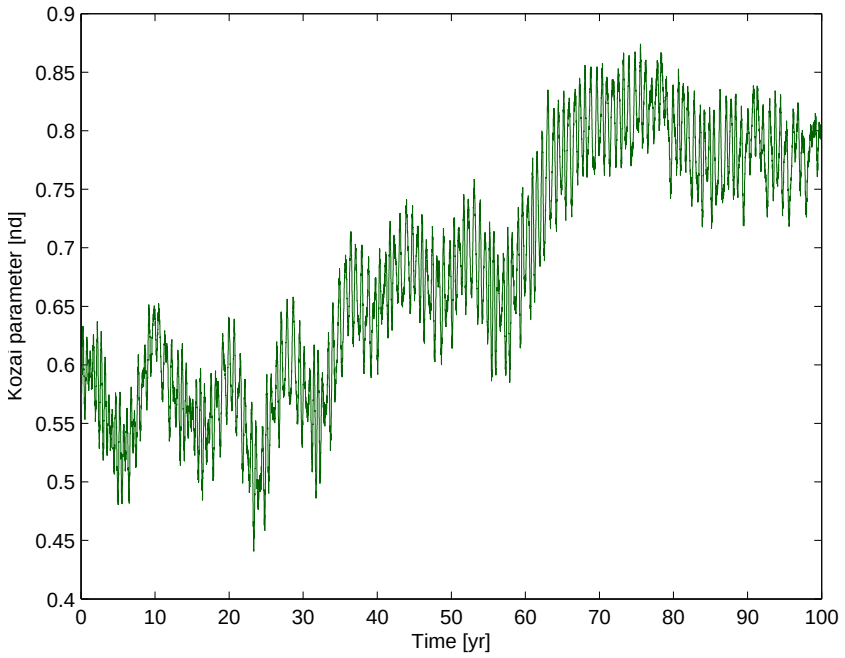

Fig. 4 Evolving Kozai Parameter for TESS-like Science Orbit (Ephemeris Model)

the TESS DRM orbit, perturbations that shift the initial state vector of the Period Adjust Maneuver (PAM) are explored. A significant percentage of perturbed trajectories display qualitatively distinct long-term behaviors and are discussed further in later sections. As an example, a single "perturbed baseline" trajectory is inspected initially. Specifically, a modest perturbation to increase the rotating-y position coupled with a corresponding decrease in the rotating-z position and a velocity change results in a particular solution characteristic of interesting behavior modes. These modes are apparent in the various panels included in Figure 5 as well as in the evolution of the Kozai parameter depicted in Figure 4. These panels, all associated with the perturbed sample trajectory, depict the evolution of each of the osculating Keplerian orbital elements. As necessary, the particular reference for each of the orbital elements is indicated. Also included in the figure is the FTLE profile introduced in Figure 3, repeated here for convenience.

There are several notable observations that can be made from the orbital elements concerning the trajectory evolution. From panel (a) in Figure 5, it is apparent that this perturbed, particular solution leads to the spacecraft r_p initially evolving above 22 r_e after about 10 years. Each of the other panels reveals, to greater or lesser degree, two additional, major transitions in behavior as the evolution approaches 40 years and just after 60 years. As the radius of perigee increases above 22 r_e after 60 years, r_a decreases to $\sim$50 r_e as seen in panel (b) consistent with the drop in eccentricity observed in panel (c). This coupled increase in distance from the Earth and decrease in distance from the lunar orbit represents additional stabilization of the spacecraft orbit. Each of these effects is reflected in the FTLE profile of panel (f). This FTLE profile, consistent with look-ahead

times of ∼1.2 years for each point, clearly indicates and summarizes the mode shifts along the trajectory while supplying a measure for stability with respect to perturbations relative to the orbit. Larger values of FTLE indicate more sensitive regions along the trajectory evolution.

The transitioning behavior observed in both Figures 4 and 5 elicits observations concerning the numerics of the analysis. The shifts around 40 and 60 years are abrupt, signaling distinctive ensuing behaviors, and require differentiation from numerical artifacts. While error associated with numerical integration is inherent in the propagation process, the sensitivity of the chaotic regime is also relevant. For example, a very small perturbation, on the order of numerical precision, is sufficient to shift neighboring trajectory evolutions into dramatically different behaviors over time. Thus, even small numerical differences will yield different solutions. To help eliminate error as a cause for the observed mode-shifting behavior, re-creation of the transitioning behavior is performed independently from its preceding numerical propagation. Additionally, system geometries and cumulative influences are explored through various methodologies to help better understand the transitions.

3.3 Frequency analysis

Inspection of the frequencies in the "signal" associated with a spacecraft trajectory can be a useful strategy to identify particular contributions to the motion of the spacecraft. For example, Bosanac et al. (2013) employ frequency analysis strategies to characterize the impact of including three-body interactions along with the inverse square pairwise contributions in a three-body system. In Figure 6, the amplitude density associated with the fundamental frequencies and some subharmonics embedded in the time-history of one acceleration component are plotted. These frequencies are associated with the y component of the spacecraft acceleration as viewed in the rotating-pulsating-librating frame that instantaneously fixes the Earth and Moon consistent with their ephemerides. Further, the frequency data are associated with the perturbed baseline trajectory that is evolved under the Sun–Earth–Moon ephemeris dynamics—the trajectory that is characterized in Figures 4 and 5. These frequency responses result from discrete Fourier transforms, implemented numerically as a Fast Fourier Transform (FFT), of overlapping data intervals initiated every four months and spanning 10 years each.

Inspection of the frequency curves in Figure 6 reveals the evolution of the frequency components. The curves are colored by the initial time of the associated FFT interval, and range from green to red. A representation of how these curves evolve for a particular frequency is shown in Figure 7. Finally, the data intervals are pre-processed using a Hanning function (Harris 1978) that yields more distinct features in the frequency spectrum. Such a windowing reduces the observed amplitudes in the signal. A few of the major accelerations associated with/acting on the trajectory are labeled. For example, the peak labeled as the 'Primary Spacecraft Period' is associated with the y component of the accelerations from the Earth and Moon gravity terms in the equations of motion. Since both the Earth and Moon are instantaneously fixed in the rotating-pulsating-librating frame, the associated peaks may be considered to emerge as reflections of interactions between the spacecraft motion and the frame that is derived by the motion of the respec-

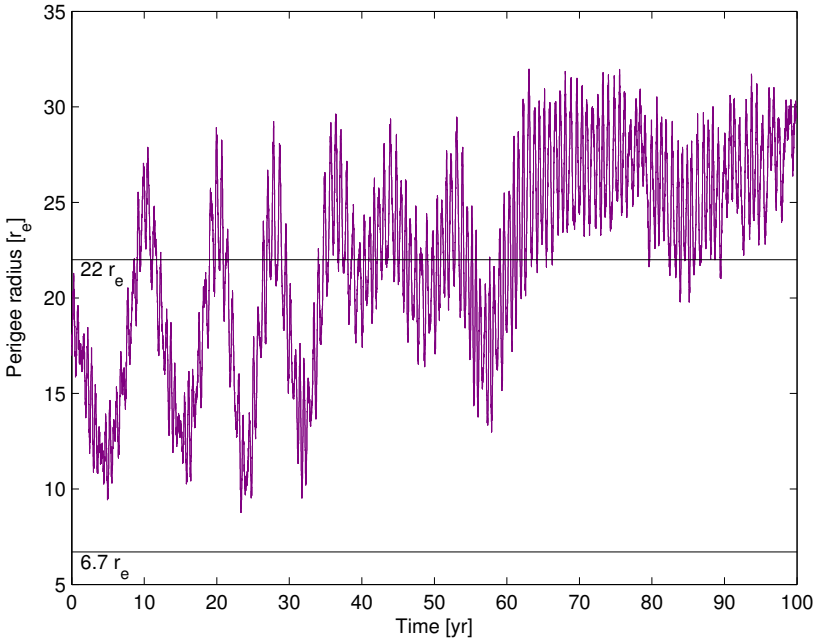
Perigee radius [r_e]
Time [yr]
22 r_e
6.7 r_e
35
30
25
20
15
10
5
0
10
20
30
40
50
60
70
80
90
100

(a)

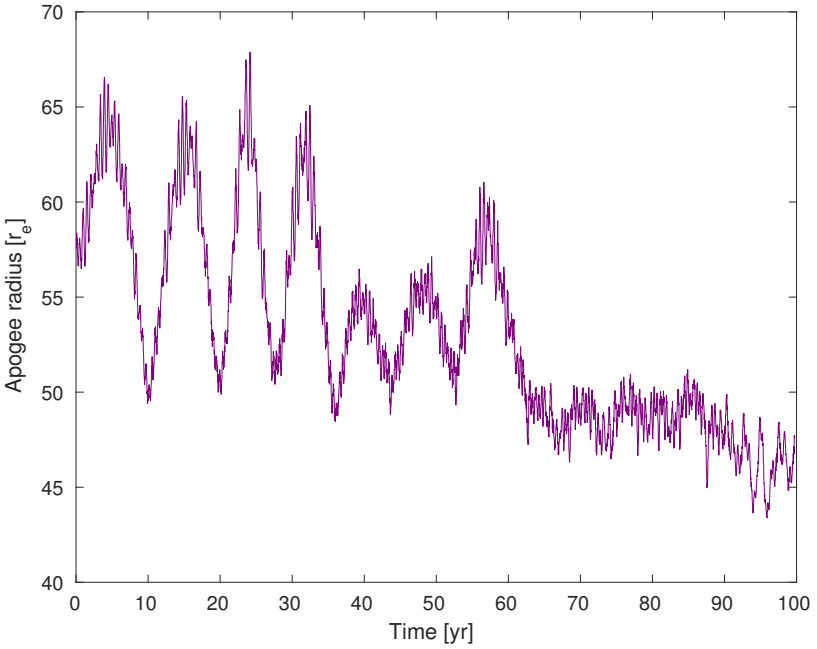
Apogee radius [r_e]
Time [yr]
70
65
60
55
50
45
40
0
10
20
30
40
50
60
70
80
90
100

(b)

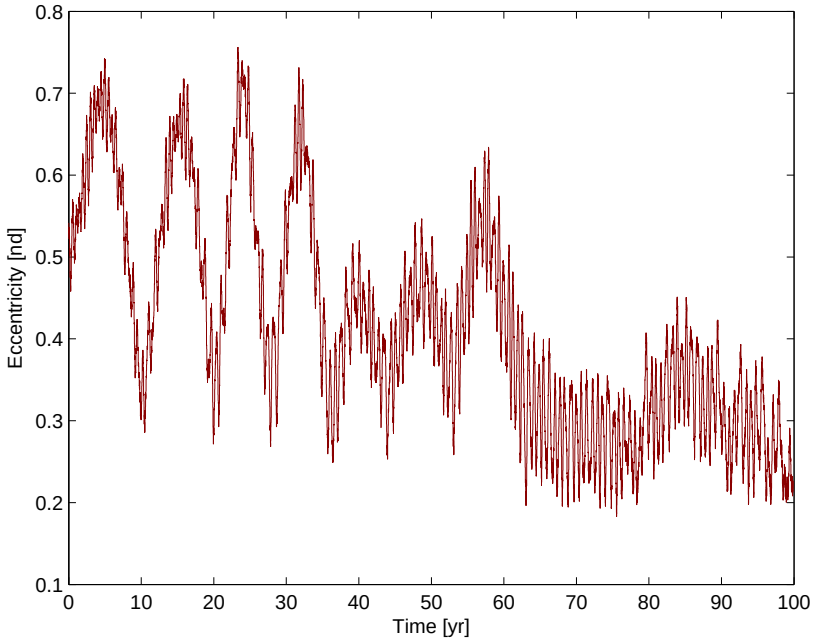
Eccentricity [nd]
Time [yr]
0.8
0.7
0.6
0.5
0.4
0.3
0.2
0.1
0
10
20
30
40
50
60
70
80
90
100

(c)

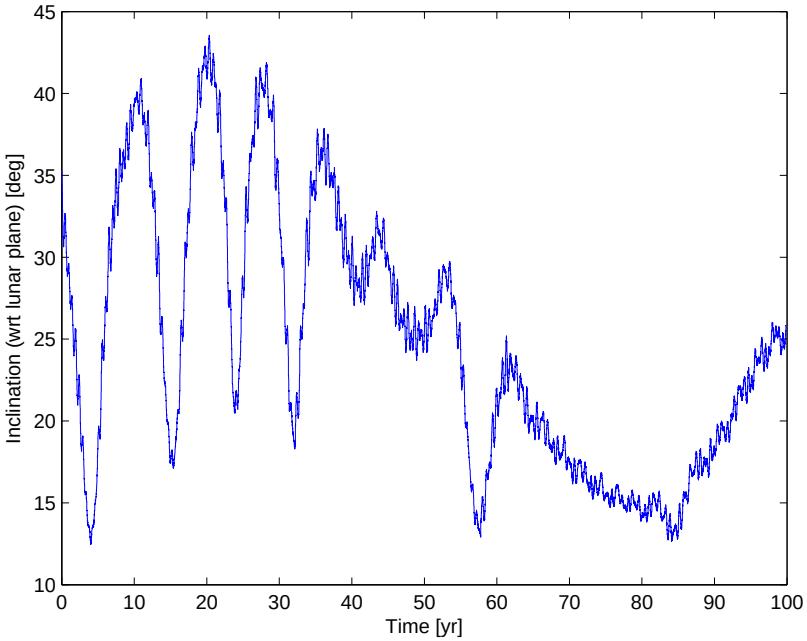
Inclination (wrt lunar plane) [deg]
Time [yr]
45
40
35
30
25
20
15
10
0
10
20
30
40
50
60
70
80
90
100

(d)

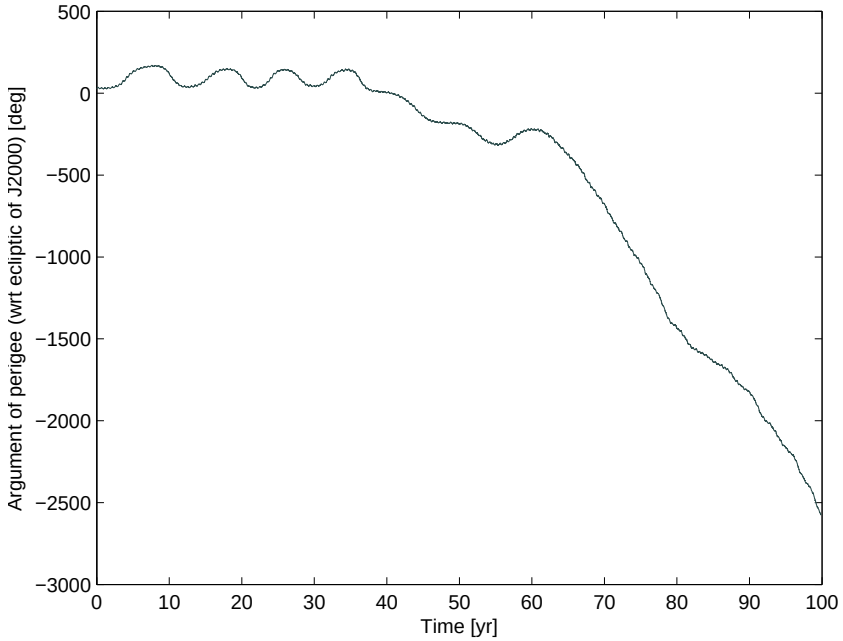

(e)

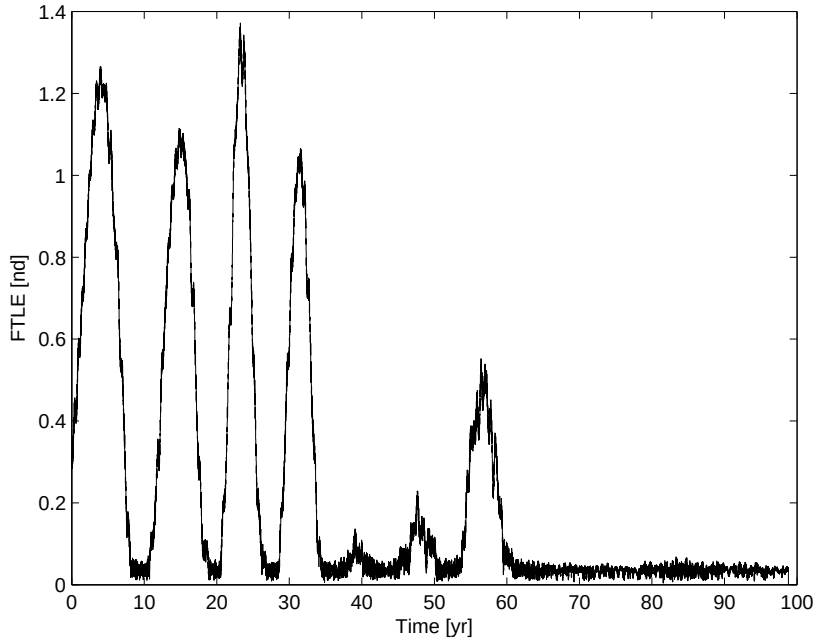

(f)

Fig. 5 Osculating Orbital Elements and FTLE Profile

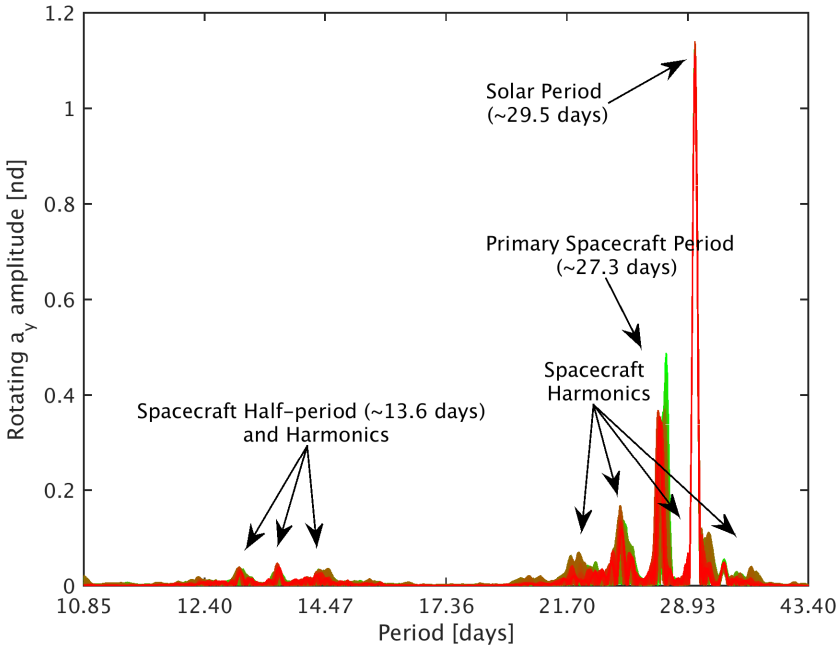

Fig. 6 Rotating Frame Frequencies in a_y from Initial 10 Years of Perturbed Baseline

tive bodies. The solar effects on the spacecraft orbit are associated with the largest peak as a consequence of the Sun's very regular, sinusoidal motion in the rotating frame. However, the peaks associated with the accelerations from the Earth and Moon are distributed into multiple harmonics, including some higher-frequency harmonics that are not plotted. This dispersion is a consequence of the evolution in trajectory behavior over time.

Tracking the amplitudes of various frequency components allows for comparisons in relative strength. As the FFT window slides forward in time the frequency response evolves. Generally, such an evolution would be rendered as a spectrogram. However, in this case, careful peak tracking is employed to inspect the changing frequency and amplitude of particular signal components. In Figure 7, a trace of the signal contribution associated with the peak corresponding to the principal spacecraft period, as it is reflected in the trajectory's a_y signal, is depicted. The underlying frequency response (plotted in terms of period) is colored according to time with earlier peaks colored in green and later peaks colored in red. As this particular peak evolves, a distinctive difference is observable both in terms of contribution strength to the overall signal as well as in terms of the period of the signal component. As is apparent in the orbital elements, distinctive modes emerge in the frequency/period trace over time. Specifically, earlier peaks colored in green are dissociated from the later ones (consistent with the terminal trajectory behavior) colored red.

The difference in signal component amplitudes over time from their initial values may be inspected. Such differences are depicted in Figure 8. Rotating x, y, and z components are plotted and each of the three peaks with indicated periods from

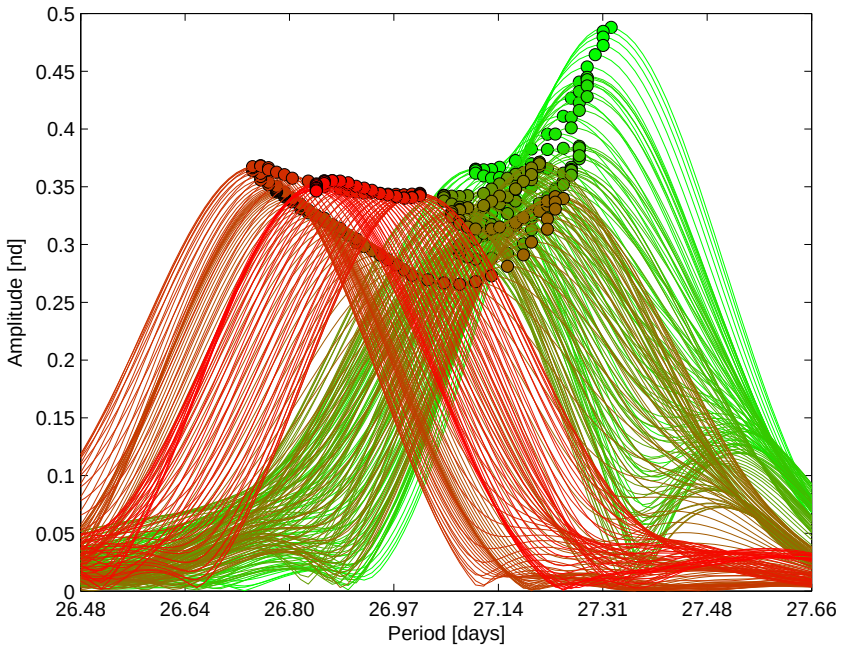

(a) Frequency Peaks Plotted as Periods

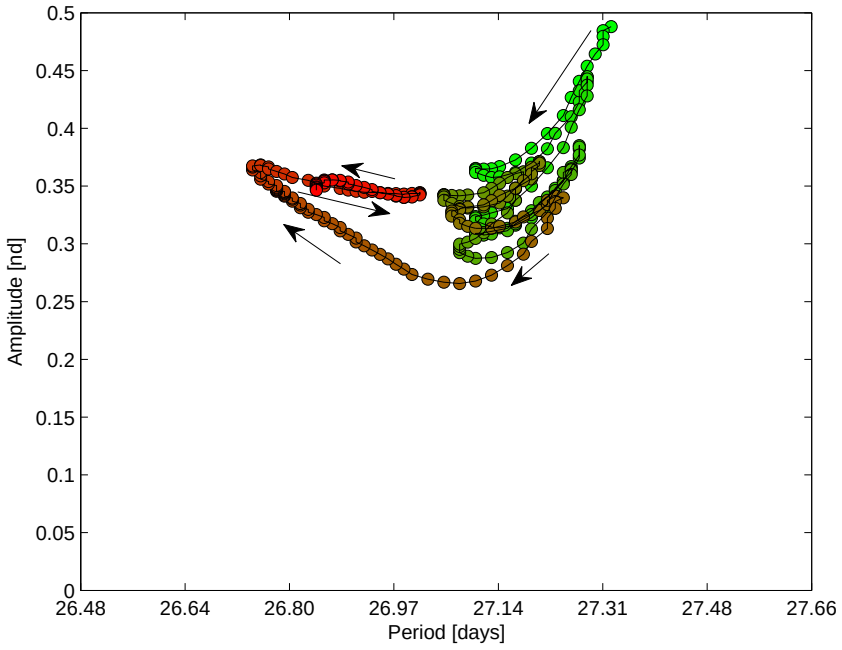

(b) Without Underlying Curves

Fig. 7 Trace of the Principal a_y Spacecraft Period (Over 90 Years; Points at 4 Month Intervals Represent FFT Results for the Subsequent 10 Years)

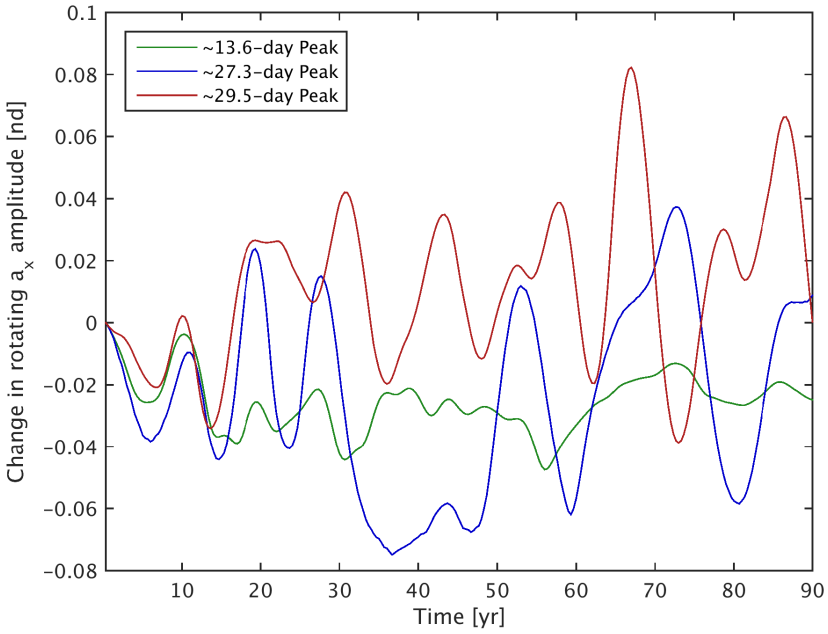

(a) From s/c a_x Signal

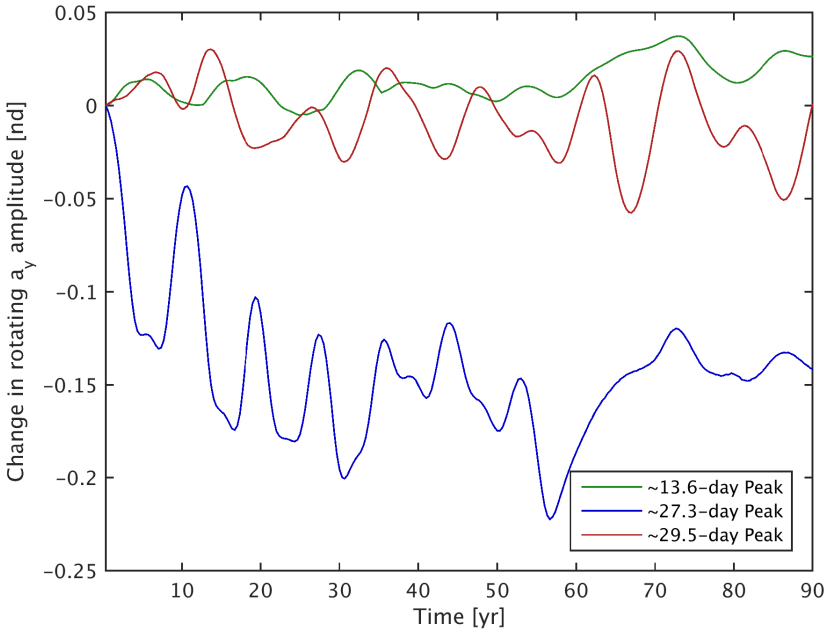

(b) From s/c a_y Signal

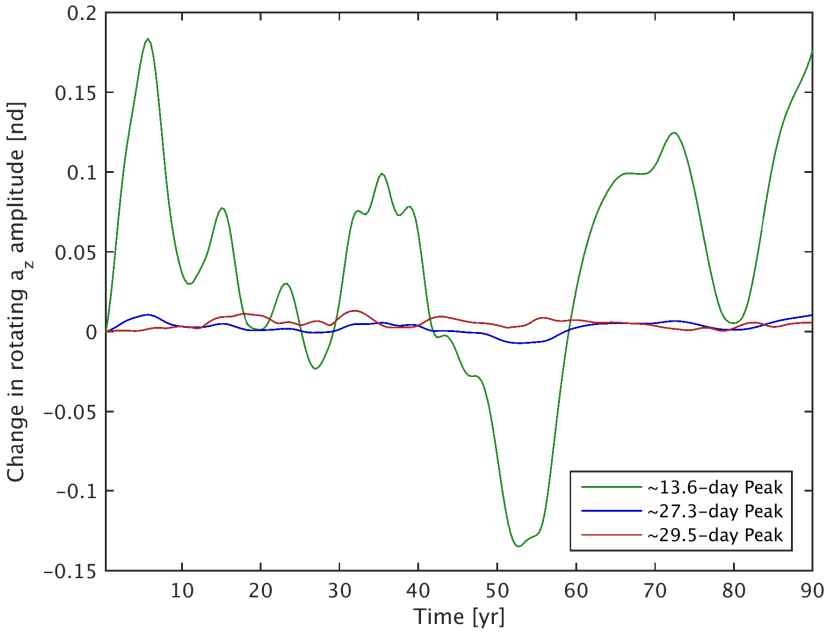

(c) From s/c a_z Signal

Fig. 8 Change in Amplitude for Three Tracked Peaks Over Time

Figure 6 is tracked over time. At each point, the subsequent 10-year evolution is invoked to construct the discrete Fourier transform. Thus, the time ranges through the first ninety years of trajectory evolution. Since the frequency evolution can be interpreted not only as the evolution of spacecraft orbital characteristics but also as a consequence of the perturbations embedded in the system, it is challenging to establish any particular behavior as driven by any single factor.

Decomposing the frequency data and comparing the associated time-histories reveals the change in the net impact of a given component. It is notable that there are periods of time when both the Earth–Moon and solar impacts in the a_x signal trade off considerably. For example, from about 30–50 years, the Earth–Moon impact seems to decrease leading into the transitioning phases seen in Figures 3 and 5 around 50–60 years. There is some correlation between the a_x signal component associated with the "half-period peak" (green line in Figure 9(a)) and the primary a_y contribution (blue line in Figure 9(b)), which indicates a more apparent coupling of these components. While there is little change in the longer-period responses of the z signal, the associated "half-period" trace is largely reflective of the spacecraft's orbital inclination seen in Figure 6(d) or, more directly, it's out-of-plane motion in the rotating frame. Further, in an a_z frequency spectrum, the ∼13.6-day period is dominant with comparable amplitudes to the ∼27.3-day peaks in Figure 6. Inspection of various frequency components lends some insight into the trajectory evolution, and additional analysis of lunar and solar contributions further expands this insight.

3.4 Additional analysis of solar and lunar contributions

Recognizing that both the Sun and Moon impart significant accelerations to the spacecraft, it is useful to inspect the interplay between these bodies in terms of both relative configurations and gravity accelerations. Observation of the relative geometries of the system at important times lends some insight. Further, a quantitative analysis of the relative impacts of lunar and solar acceleration contributions supports the conclusion that the evolution of the spacecraft motion is a reflection of a coupling between the two perturbative influences.

While the general motion of the spacecraft is dominated by the influence of the Earth, neither the Moon nor the Sun can be neglected when attempting to understand the evolution of the associated orbit. Working backward from the epoch (September 20, 2017) associated with the PAM of the science orbit characterized in Figures 4–8, the early mission timeline and associated system geometry may be extrapolated. In Figure 9, the Sun's general direction is indicated graphically for particular events in the early phases of the DRM. The figure is depicted in the Earth–Moon rotating frame, and the central inset of the DRM is borrowed from Dichmann et al. (2014). For each of the apoapses during the phasing loops, the

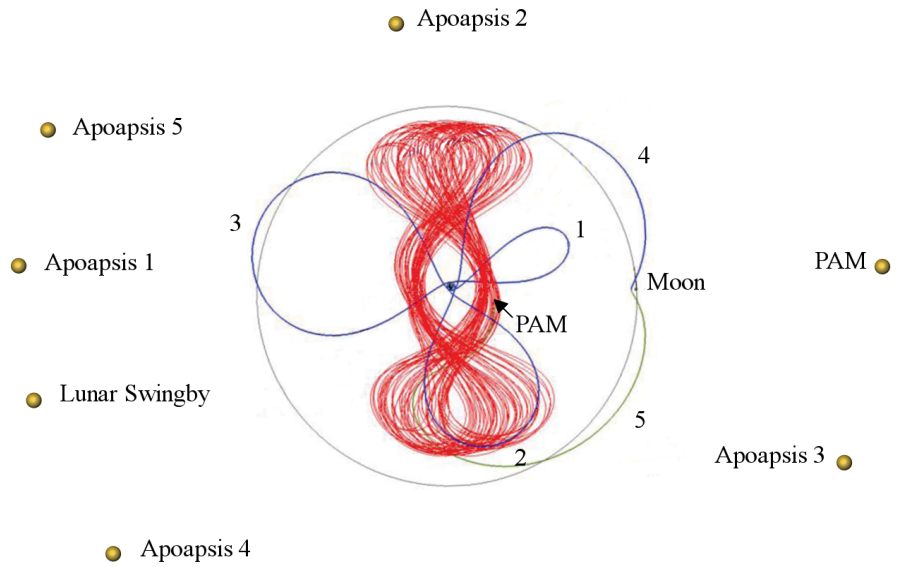

Fig. 9 Sun Directions in the Earth–Moon Rotating Frame for Early DRM Events

Sun is located generally opposite the Earth from the spacecraft. This configuration is also maintained for the lunar swingby, but not for the period adjust maneuver where the Sun is on the same side of the Earth as the spacecraft. For all of the configurations in the figure, the spacecraft, Earth and Sun lie very roughly along the same line, and for the cases where this linear alignment is less accurate (e.g., apoapses 1 and 2) the spacecraft altitude is generally lower where the solar influence is decreased.

The solar impact on the trajectory can be identified from the Sun's relative position in the system. While the system geometry as depicted in the rotating frame reflects various solar positions, the solar motion in the Earth-centered inertial frame is relatively small. However, viewing the geometry in the rotating frame establishes how the Sun effects the trajectory at apoapses as described by Howell and Craig Davis (2008). Linear orientations of the Sun, Earth and spacecraft at apoapsis induce minimal change in the spacecraft's orbital elements from the solar influence. As the spacecraft moves into the science phase, the solar direction does not maintain a particular orientation in the rotating frame for trajectory apoapses. During the science phase the solar direction fills out a circular band at the solar distance from the barycenter of the rotating frame, and extends above and below the x–y plane of the rotating frame consistent with lunar orbital inclination.

A quantitative comparison of the accelerations imparted to the spacecraft from the Sun and the Moon aids in demonstrating that the trajectory behavior is a general reflection of all combined effects. Prado employs an approach to determine the total contribution of a particular perturbative effect over time by integrating the associated acceleration components (Prado 2013, 2014). Sanchez (2014) further employs and expands this methodology. The cumulative effect of a particular perturbation over the time-interval, $I := [t_i, t_i + T]$, in a given direction may be calculated by integrating, $p_j = \int_{t_i}^{t_i+T} a_j \, dt$, where a_j is the acceleration component corresponding to the perturbation along the specific direction coordinate j, t_i is some initial time and T is some later time (in this case, T is a time horizon similar to that employed for computing $\mathbf{C}$). Moreover, the total impact of the perturbation is then computed as $p = \int_{t_i}^{t_i+T} |\mathbf{a}| \, dt$, and the energy imparted to or removed from the spacecraft motion by the perturbation is evaluated as $\Delta E = \int_{t_i}^{t_i+T} \mathbf{a} \cdot \mathbf{v} \, dt$.

Computing the various perturbation integrals establishes the relative contributions of each perturbation. All of the integrals are computed using J2000 ECI dimensional coordinates for this analysis. Invoking a sliding time-scale as used for computations in preceding sections, the traces in Figure 10 depict the integrated accelerations along the perturbed baseline solution corresponding to each component. At each time step, the subsequent ten years of acceleration data are integrated and plotted. The integrated acceleration components acting on the spacecraft due to lunar gravity, as seen in the ECI J2000 reference frame, appear in Figure 10(a) while the solar counterparts are plotted in Figure 10(b). Consistent with the more stable trajectory behavior observed from 30–50 years and again beginning around 60 years during the evolution, many of the component-wise acceleration contributions from both the Sun and the Moon are observed to experience periods of generally lower magnitude. During the transition in behavior that is apparently triggered at around 60 years, the solar perturbations are observed to pass through a phase of minimal contribution to the motion. This minimal phase, coupled with the lowered influence imparted from the Moon during the same time frame marks the initiation of the subsequent increased stability phase of the trajectory behavior.

Comparing the overall solar and lunar perturbation contributions in terms of both magnitude as well as alignment with the spacecraft velocity vector reveals additional insight. In Figure 11, the magnitude of the lunar and solar accelerations are integrated, again employing a ten-year sliding time interval. In general, the lunar influence is observed to be approximately double that of the solar influence

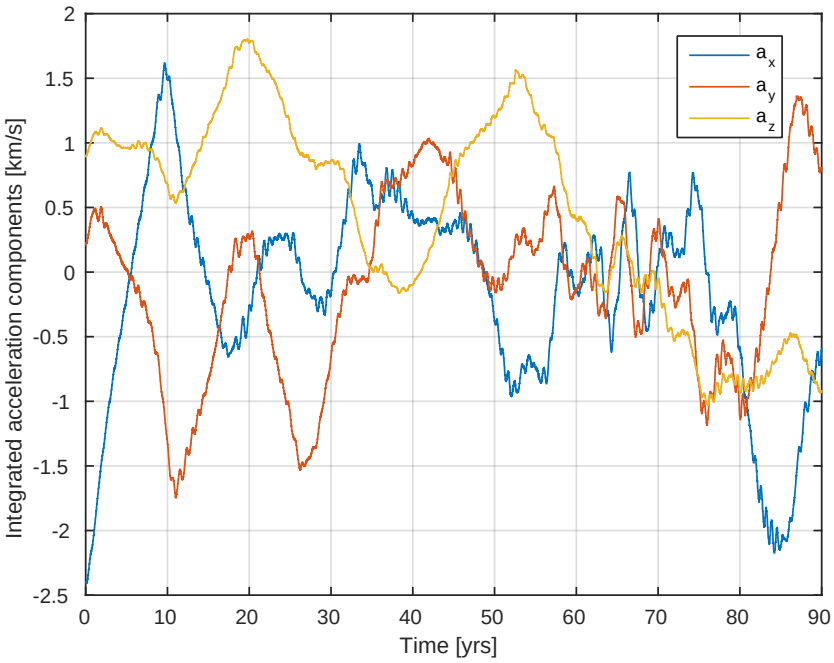

(a) Lunar Acceleration Components

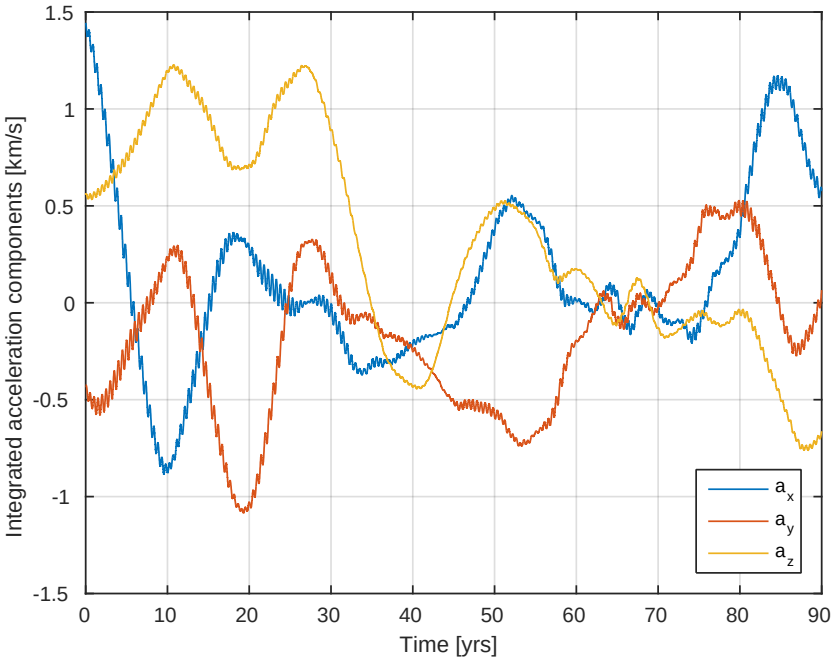

(b) Solar Acceleration Components

Fig. 10 Sliding 10-Year Integrals of Gravity Perturbations on the Spacecraft (J2000)

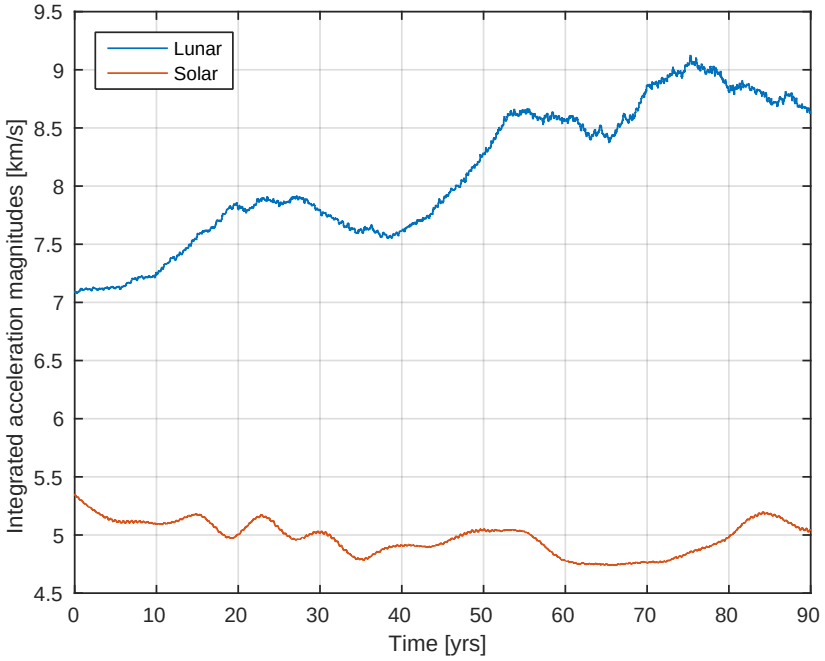

Fig. 11 Overall Solar and Lunar Perturbative Contributions to the Motion

over the 90-year interval and displays an increasing trend over time. Periods of local minimal contribution appear consistently with the component-wise results observed in Figure 10. Finally, the transition at around 60 years along the science orbit evolution is illustrated well by the ΔE integral, i.e., $\int \mathbf{a}\cdot\mathbf{v}\, dt$, again evaluated for the subsequent 10-year interval originating at each plotted point in Figure 12. Initially, the solar contribution over each subsequent ten-year interval imparts energy to the spacecraft motion. The lunar influence fluctuates more rapidly over this time frame, but it removes energy from the spacecraft motion on average. This lunar trend gradually decreases over time (i.e., the Moon's acceleration on the spacecraft and the spacecraft's velocity direction slowly begin to align). As the spacecraft evolution approaches 60 years, the average lunar influence shifts to impart energy to the spacecraft motion accompanied by an uptick in the solar contribution. At this point, the de facto equilibrium imparted by the lunar and solar perturbations inverts as the general system behavior changes and the trajectory enters a more stable phase for a few decades. The spacecraft trajectory in this particular perturbed baseline case will eventually evolve out of this more stable phase. Comparisons of the individual lunar and solar perturbative contributions indicate that the general trends in behavior are a cumulative reflection of all the model components. Further exploration of these components and nearby solutions reveals that the trends are very sensitive to small initial variations.

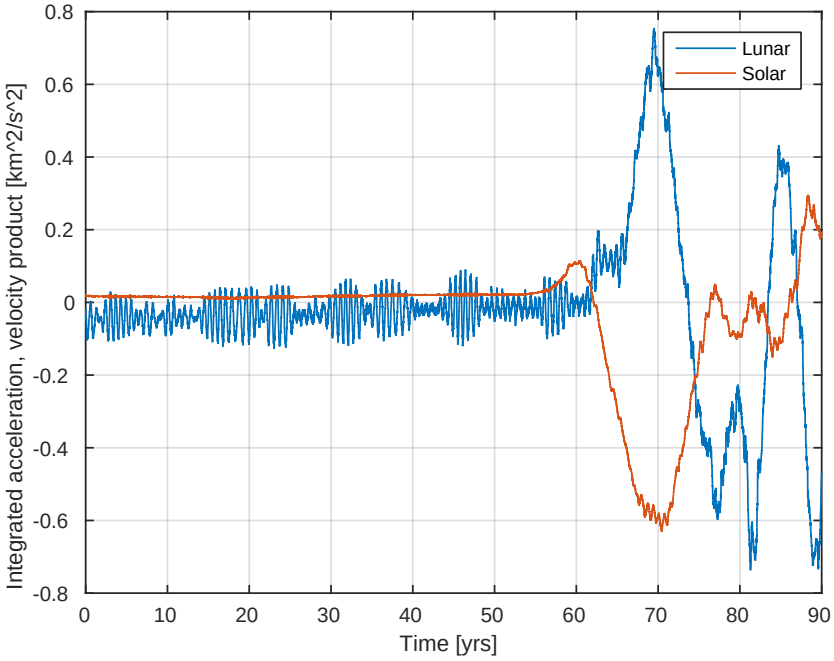

Fig. 12 Specific Energy Imparted to the Spacecraft Over Time

3.5 Model component analysis

Comparison of the different components that influence the motion along the path yields some insight into the behavior. However, the goal is to identify particular aspects of the model that drive the trajectory into a given mode, thus, this analysis must be performed relative to a solution displaying the behavior of interest. Since the CG tensor is model-agnostic, evolution of a particular initial state under the influence of different systems allows for the comparison of flow metrics that are derived from the Cauchy–Green tensor. In particular, the FTLE values computed along the trajectory may be compared to indicate a sense of the flow behavior. For these calculations, it is necessary to periodically reset the initial states for the lower-fidelity models to remain along the trajectory of interest. Consider the following strategy:

1. Calculate the baseline trajectory (generated from an initial condition of interest perturbed from the TESS DRM state) by evolving under the higher-fidelity ephemeris model, and retain intermediate states at specified intervals, regularly spaced in time.
2. For each of the intermediate points along the baseline path, calculate the CG tensor for the length of the given time interval.
3. In addition, transform the baseline state as appropriate to conform to lower-fidelity models.
4. Compute the STM under the lower-fidelity dynamics for each state.

5. Transform the STM as necessary to match the reference frame associated with the baseline, and compute the CGST and FTLE values.

By computing FTLE values for the baseline trajectory and then removing model components and computing comparative values, the impacts of some effects are captured. Selecting an appropriate time scale for discretizing the baseline path is a critical consideration so that the influence of the reduced models is allowed sufficient time to be observable without completely diverging. It is possible to impose smaller discretization steps and multiply the resulting state transition matrices to form a composite STM over a longer time interval; but, this method must also be approached with caution since a time slice that is too small may not allow the individual lower-fidelity effects to be discernible.

A comparative FTLE analysis is generally sensitive to the selection of both the integration and normalization times for the FTLE. Some intuition or experimentation is usually required to determine an adequate time scale. For the present calculations, time slices are collected at each 0.025 nd time steps and composited to create an STM equivalent to one produced from ∼1.2 years (100 nd) of evolution. Experimentation with other time scales for slicing and compositing suggests that the present set of parameters represents an acceptable trade-off for meaningful comparisons. Traces of FTLE values associated with five separate model formulations using the given time horizon are included in Figure 13.

From Figure 13, it is immediately apparent that two general groupings of behavior emerge, that is, one group associated with lower-fidelity models and the other with the more realistic ephemeris options. Insets associated with the regions isolated with magenta (a) and red (b) boxes are included in Figure 13 to aid these comparisons. Embedded in the ephemeris options are many higher-order perturbative effects that are not captured by the circular restricted, elliptic restricted, and bicircular restricted problems. While general consistencies are apparent in the long-term behavior as the several large peaks and troughs appear correlated between lower- and higher-fidelity models, ultimately, over the prescribed time scales, the lower-fidelity models struggle to capture the combined cumulative effects of higher-order perturbations. It is also apparent that the addition of the fourth-body perturbation appears to produce a lesser effect than the introduction of other components of the lunar orbit. For example, compare the blue and red traces of inset (a) as well as the teal and black lines in inset (b) in Figure 13 (both sets generally overlap) to note the relatively small difference associated with introducing the fourth body (the Sun) into the model. Alternatively, the green and red data in inset (a) reflect the elliptic effects of the lunar orbit.

Given the close association between the Earth–Moon ephemeris and the Earth–Moon–Sun ephemeris traces (teal and black), a reasonable conclusion is that the Earth–Moon dynamics are generally more significant, and the cumulative effect of the higher-order perturbations in lunar motion may play a larger role in this particular scenario. Further examination of such perturbations and model components suggests that the problem sensitivity over longer times is a critical component in the trajectory behavior, potentially sufficient to overshadow any individual contributing factor, as illustrated by inspection of nearby solutions.

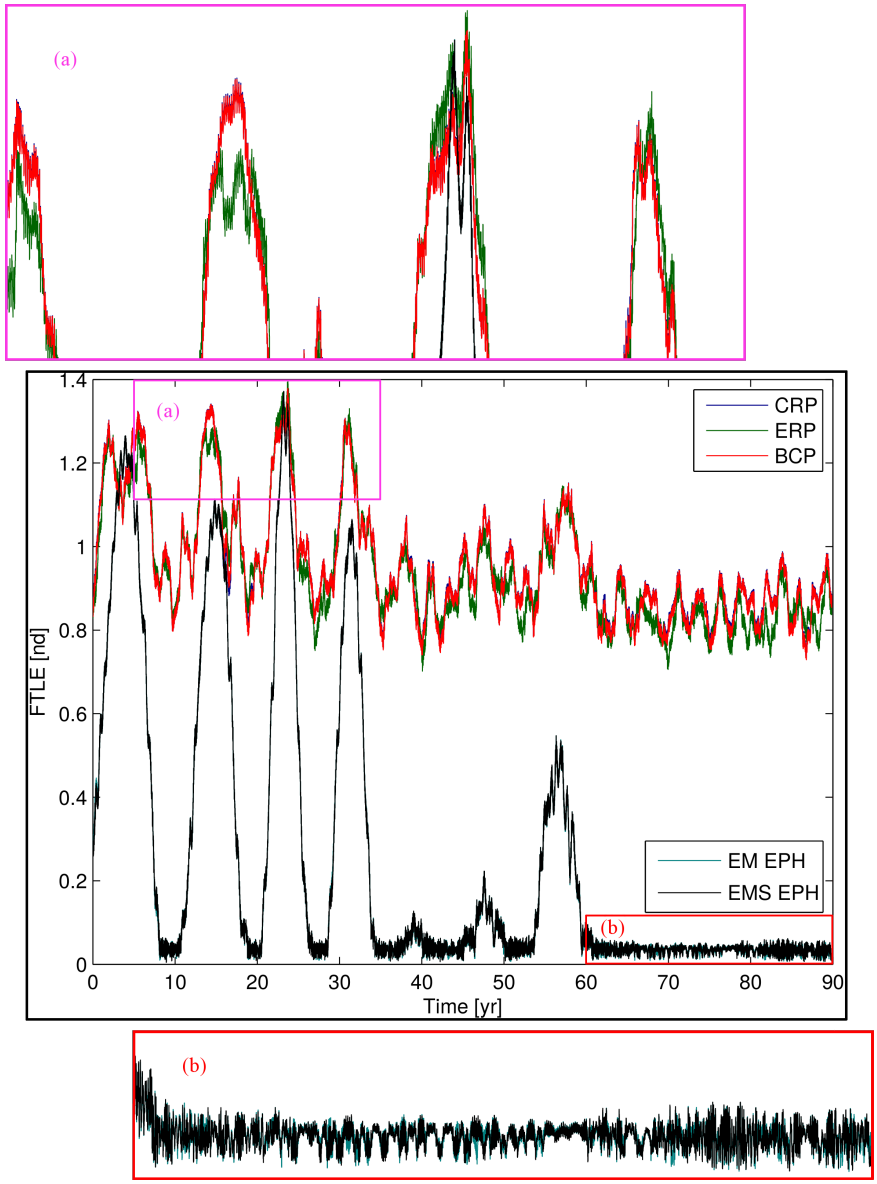

Fig. 13 FTLE Profiles for Ephemeris Baseline (Black) and Reduced-Fidelity Propagations

3.6 Nearby solutions and FTLE profiles

Further exploration in the phase space nearby the initial conditions associated with the perturbed baseline solution as characterized in Figures 4 and 5 adds compelling insight into the trajectory behavior. Various strategies for such an inspection are available. Rather than employing random nearby initial states or using a grid-based strategy, a flow-based approach is adopted. In general, the natural

flow in the system will rapidly align with the largest stretching direction in the phase space. Thus, seeding initial states along the eigendirection associated with the largest eigenvalue from the Cauchy–Green tensor allows for a one-dimensional search direction that will most efficiently spread throughout the phase space. The CGST is evaluated from the initial state for increasing time horizons until the largest eigenvector, $\boldsymbol{\xi}_n$, stabilizes and before the computation numerically overflows. A time horizon of 100 nd time steps is sufficient to accomplish this numerical balance. The search, then, is *designed to maximize the divergence* from the initial state, and the subsequent evolution is associated with the long-term behavior of the set of seeded trajectories.

A mapping of several FTLE traces provides contextual information for the long-term trajectory behavior. Recall the FTLE profile depicted initially in Figure 3; such a profile may be viewed as a one-dimensional track colored by relative FTLE values and the profile from Figure 3 corresponds to the "row" marked as zero along the vertical axis in Figure 14 where lower-to-higher FTLE values are

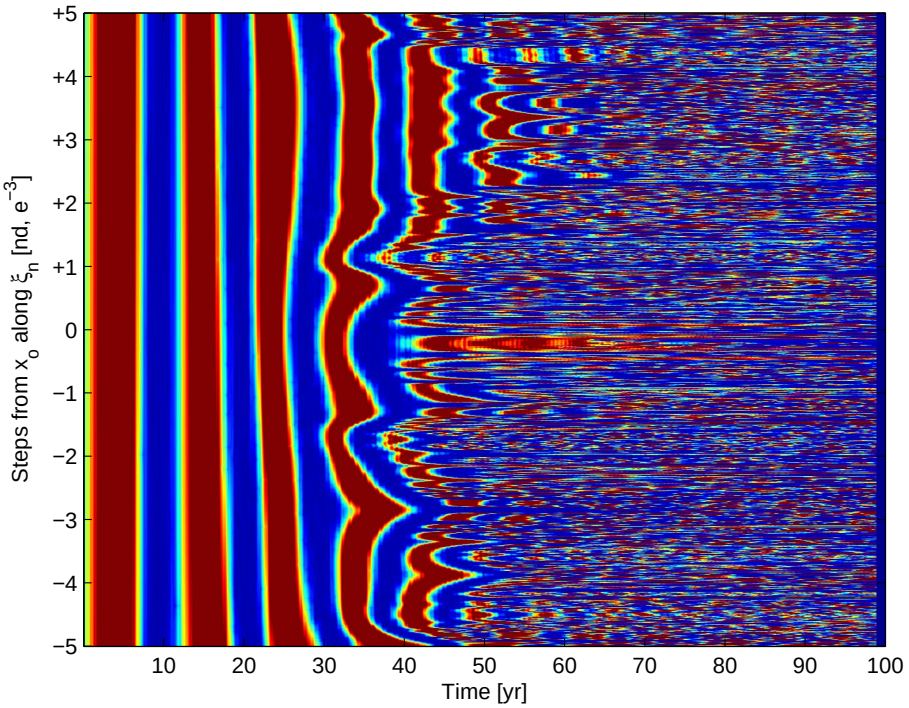

Fig. 14 FTLE Profiles from the Baseline (Vertical Axis: 0) and Perturbations Along $\pm\boldsymbol{\xi}_n$

colored using a blue-to-red spectrum color mapping. Five hundred steps along both the $\pm$ directions in $\boldsymbol{\xi}_n$ are tagged as initial state vectors to form the search set. Each step is characteristic of a nondimensional step size of 1×10^{-5}. For reference, in position, 1×10^{-5} nd ≈ 3.84 km while 1×10^{-5} nd $\approx 1.02\times10^{-2}$ $\frac{\text{m}}{\text{s}}$ in terms of velocity, but a step along the eigendirection is distributed, likely unequally, in both position and velocity. The four initial peaks observed in the previous plots (e.g.,

Figure 3) generally persist under the specified perturbations and are observed as thick red bands in Figure 14. It is apparent that sometime between 40–60 years, the solution space becomes generally unpredictable, as the map bleeds into noise. This time frame correlates to notable shifts in behavior along the original baseline path. The transition into noisy behavior is a consequence of the chaotic regime, and is a reflection of the sensitive dependence on the initial conditions. This sensitivity must also be considered within the context of numerical integration error. For example, a variance in the last digit of only one state component from an initial condition (given to double precision) may be sufficient to shift a solution into behavior consistent with a neighboring perturbation after several decades of propagation. Further analysis, including additional propagations initiated near transitioning phases, is performed to ensure that the behaviors are, in fact, dynamical and not a reflection of numerics.

3.7 Conditions for entering more stable modes

At the conclusion of the science phase of the TESS mission, it may be desirable to evolve the trajectory into a more constant "disposal mode" described by lower eccentricity and higher periapse altitude. Such a trajectory is consistent with the later phases of the perturbed baseline solution investigated in this analysis (Figures 3 and 5). With some insight into the dynamical context and the associated complexity, it is possible to isolate conditions for a solution that mimics the terminal phase of the perturbed baseline. Beginning near the peak at $\sim$57 years in Figure 3, the subsequent behavior in the nearby phase space is plotted as an FTLE profile map in Figure 15. In this case, larger (but fewer) steps along $\boldsymbol{\xi}_n$ are tagged ($\pm$100 steps of size 1×10^{-4} are traversed).

The plot in Figure 15 illustrates a few key observations. First, relatively small perturbations drastically shift the behavior—this fact is more pronounced since the perturbations are induced near the top of a modest FTLE peak (a more sensitive placement). A strip of relatively tame FTLE values (dark blue) is observed near the baseline (ordinate: 0) and persists for a few steps along the negative $\boldsymbol{\xi}_n$ extension. However, perturbing slightly further along the negative $\boldsymbol{\xi}_n$ direction produces profiles with "flat", cerulean FTLE values. These values, despite their calming coloring, are consistent with trajectories that have been ejected from the local neighborhood leading to FTLE stabilizations as the trajectory essentially orbits the Earth–Moon system (in a rotating perspective). This particular plot helps to characterize the nearby behavior after transition.

As a consequence of the observations from Figure 15, solutions reflecting transition into alternate modes are now sought earlier along the evolving trajectory path. To begin this process, an initial state is sought that minimizes the difference between the relative system orientation of the spacecraft, the Earth, the Moon and the Sun with respect to some later configuration that demonstrates desirable behavior. The inertial positions and velocities of the system components may not actually be equal to their respective values at the later time, but the overall relative system configuration should match as closely as possible. For example, conditions are sought such that the difference in the magnitude of the relative state vectors

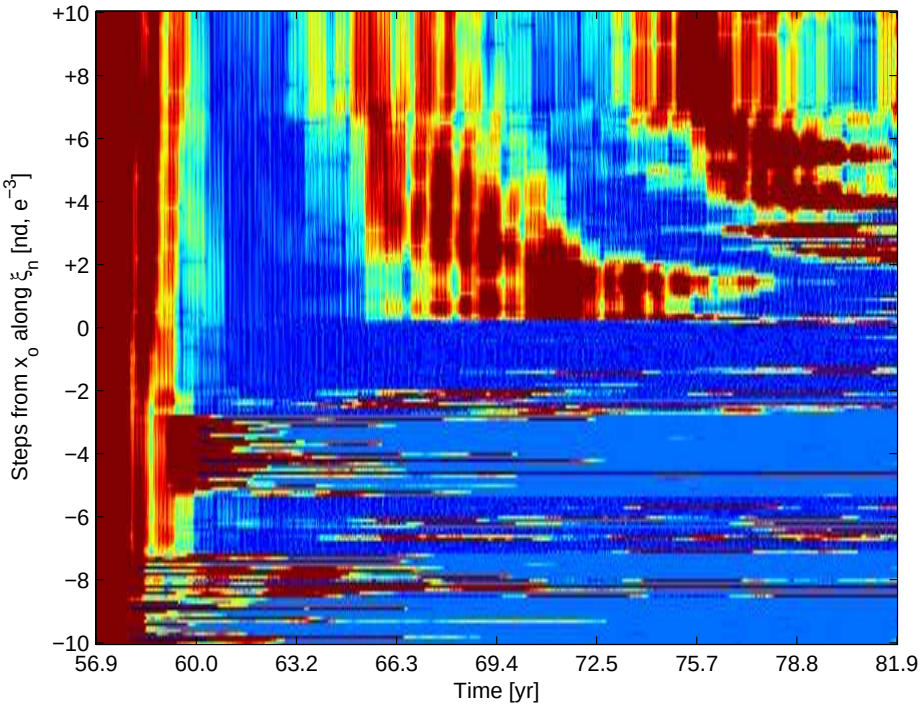

Fig. 15 FTLE Profiles, Baseline and Perturbations Just Prior to Transition Around 60 Years

between the spacecraft and the Moon at two times is minimized, i.e.,

$$\Delta_{\mathrm{sM}} = \left| \left(\boldsymbol{x}_{t^*}^{\mathrm{s/c}} - \boldsymbol{x}_{t^*}^{\mathrm{Moon}} \right) - \left(\boldsymbol{x}_{t}^{\mathrm{s/c}} - \boldsymbol{x}_{t}^{\mathrm{Moon}} \right) \right|, \tag{12}$$

where values at time t^* are characteristic of desirable trajectory behavior. This process is repeated with respect to the Sun's relative configuration and, then, a weighted averaging that most closely satisfies all constraints is isolated at a specific time. In the process of seeking conditions consistent with Equation 12 and the analogous solar conditions, the spacecraft state is necessarily adjusted in position and velocity. Consequently, an upstream maneuver would be required to achieve the associated averaged spacecraft state. One such averaged state is identified at 7.77 years as the trajectory evolves into the first FTLE trough in Figure 5(f). The FTLE profile map associated with the *unaveraged*, baseline state and perturbations is included in Figure 16. Without adjusting the state to meet the necessary geometric constraints, the FTLE evolution is reflective of the peak-and-trough behavior along the baseline, however, some differences between Figures 14 and 16 are expected because $\boldsymbol{\xi}_n$ is computed at the later epoch. Alternatively, employing the *averaged* state, the landscape appears significantly different, as is apparent in Figure 17.

Several features are notable in Figure 17. First, as also observed in Figure 14, transitioning into the later modes is characterized by an apparent increase in chaoticity of the system likely associated with an energy change at the transition. In the case associated with Figure 17, *the transitioning behavior is in-*

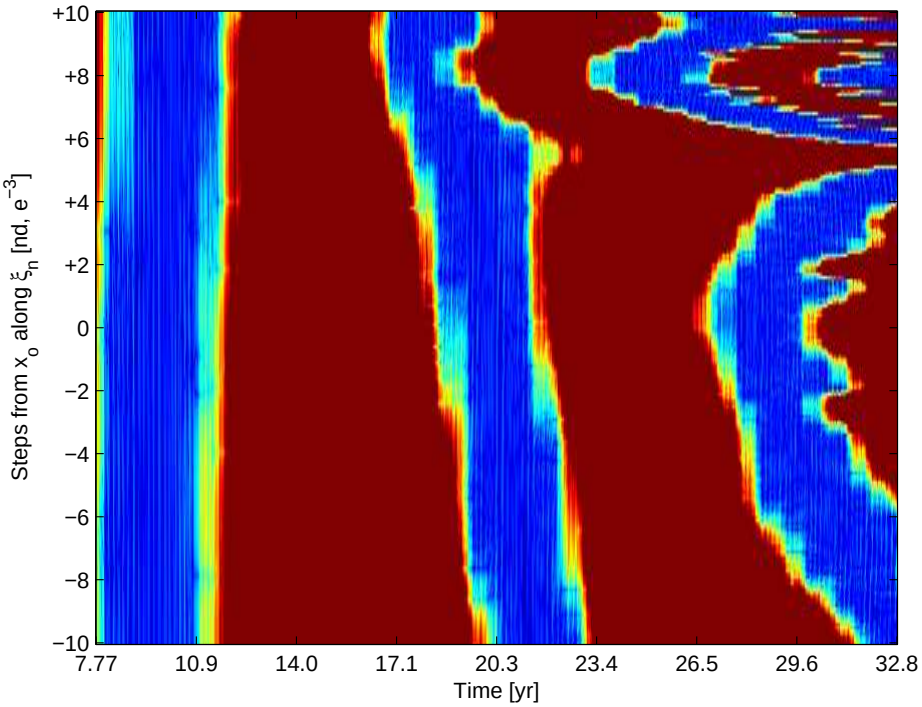

Fig. 16 Unaveraged, Baseline and Perturbation FTLE Traces

duced much earlier and the resulting FTLE field is populated with several profiles that flatten out consistent with escapes (again, characteristic of cerulean coloring). In general, darker blue FTLE values are consistent with more stable behavior and several profiles reflect such values as well. A particular contiguous region of dark blue traces that run through the perturbations ranging $\boldsymbol{x}_{\mathrm{o}} + \left(-5 \times 10^{-3} > \boldsymbol{\Delta} \cdot \boldsymbol{\xi}_n > -25 \times 10^{-3}\right)$ is also noted. Traces characteristic of such FTLE profiles are reflective of the mode behavior observed in the terminal phase of the original perturbed baseline solution, and they persist for several decades in many cases. Moreover, interspersed throughout the entire map, roughly 4% of the trajectories maintain the ideal FTLE signatures with slight or no deviations. For example, consider the FTLE trace included as Figure 18(a) that results from a solution that has been propagated from initial conditions defined from a step equal to $-0.0121 \times \boldsymbol{\xi}_n$. The plot's vertical axis is held to scale with Figure 5(f) for comparison, and the FTLE data for the first 7.77 years from Figure 5(f) is also included prior to the red dashed line, where the perturbed state is invoked. The associated radius history is plotted in Figure 18(b). In general, the spacecraft perigee and apogee radii are further from the Earth and Moon, respectively, lessening the associated impact of perturbations from these bodies.

By inducing transitioning behavior earlier in the mission time-frame, potential long-term, increased stability options are available. A specific example associated with the FTLE trace from Figure 18(a) initiates 7.77 years after the beginning of the TESS mission, and the 100-year evolution of this solution is included in

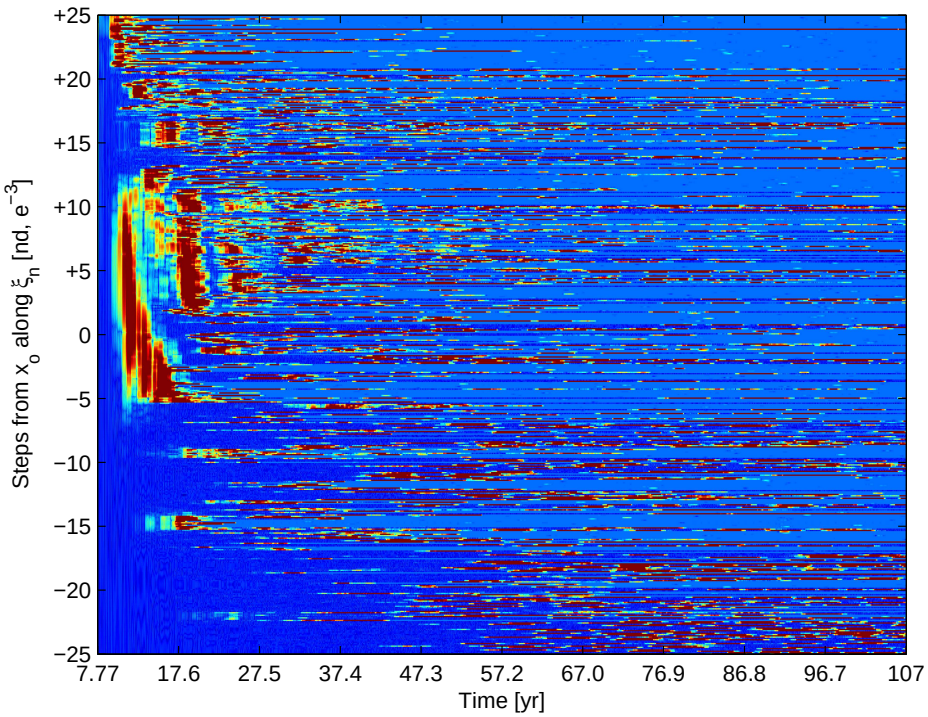

Fig. 17 Averaged State and Perturbation FTLE Traces

Figure 19. This orbit generally fills out a bounded shell in the rotating frame and serves as an example resulting from the process detailed here. The orbit is observed to evolve through various modes apparent through the coloring in Figure 19. As the orbit continues through its 100-year propagation, the coloring ranges from initial phases represented in blue through intermediate stages with mid-spectrum colors of yellow and green and ultimately concludes with red coloring interior to the shell traced out by earlier revolutions. The overall evolution is characterized by increased r_p with respect to the Earth while maintaining a modest upper bound on r_a as the orbit maintains an adequate distance from the Moon. Such a solution represents many possible options that may be isolated through numerical exploration of perturbations strategically placed in time. These options are isolated by (1) identifying specific modal behavior exhibited by perturbed solutions, (2) seeking similar system configurations at other times within the path evolution, and (3) searching the flow behavior of the nearby phase space to identify potential trajectory responses.

The selected science orbit for the TESS DRM supplies an effective end-of-life option with a dispose-in-place strategy. However, the sensitive operating regime allows for the possibility of transitions in the long-term spacecraft trajectory behavior that may or may not be acceptable. Greater knowledge of the complex environment in the vicinity of such a solution can lead to other, useful options. In the example highlighted in this analysis, particular solutions characterized by notable long-term behavior may be realized by identifying a particularly advanta-

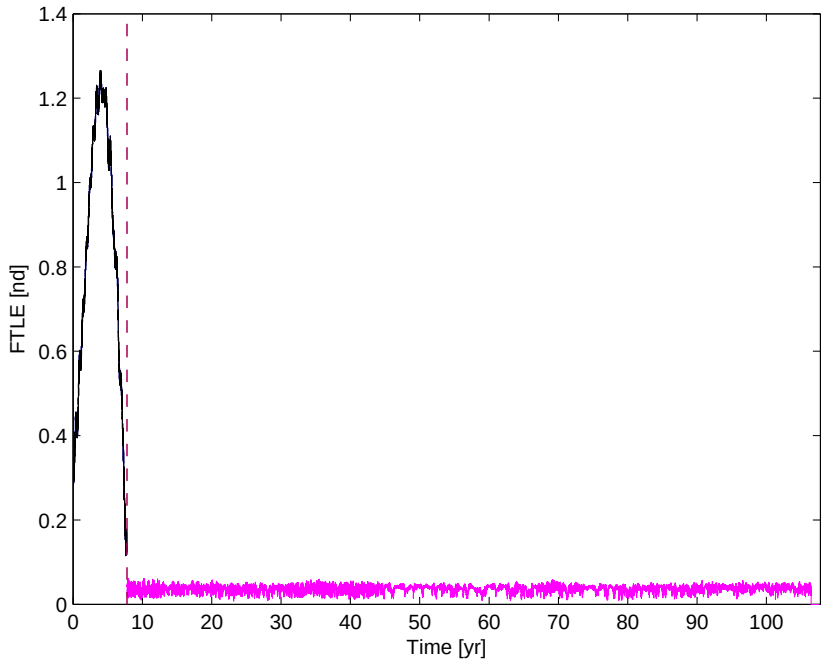

(a)

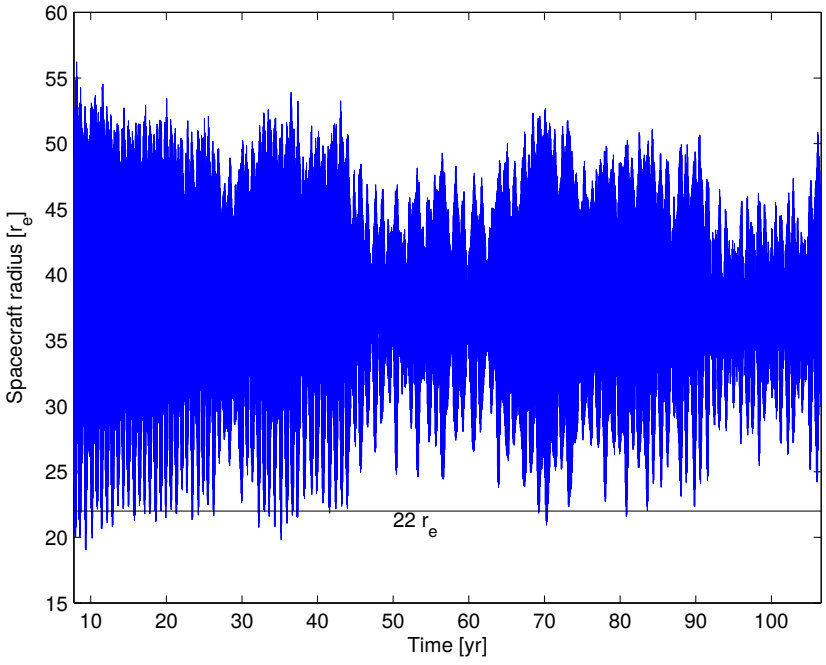

(b)

Fig. 18 FTLE Trace and Radius Profile from Perturbation to Averaged State

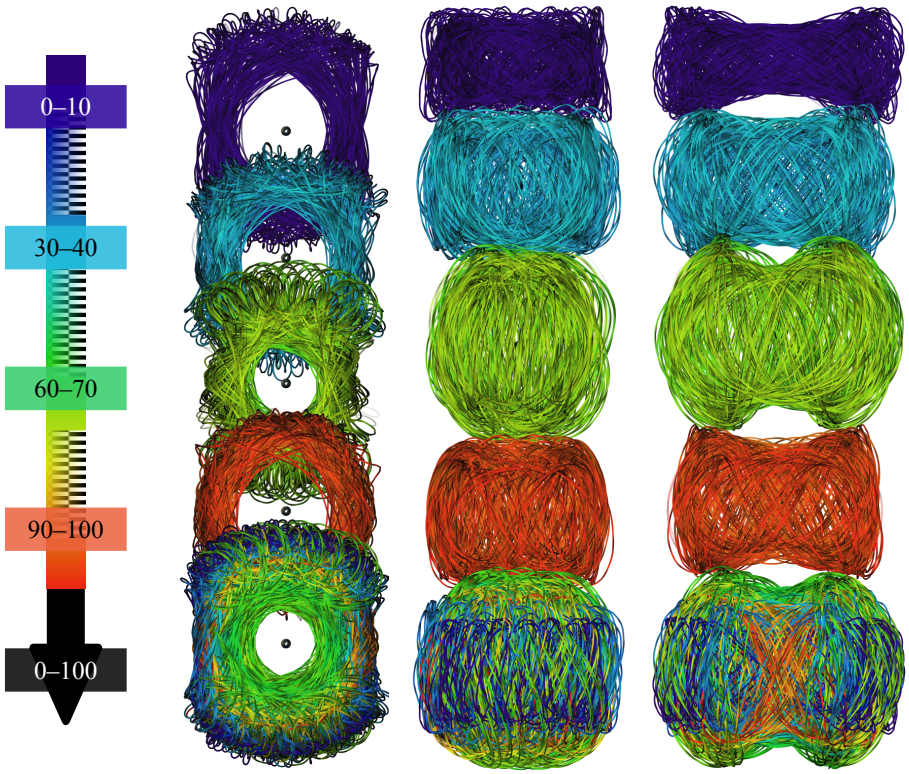

(a) Time [yr–7.8] (b) x–y View (c) x–z View (d) y–z View

Fig. 19 100-Year Ephemeris Evolution of Orbit from Figure 18 (Rotating Frame View)

geous epoch for shifting into alternate modes and perturbing the spacecraft state to accomplish evolution into the new option. Such an engineered transition would likely require planning to execute one or more maneuvers at an earlier epoch along the trajectory evolution and, while likely feasible, would warrant additional analysis and assessment.

4 Concluding Remarks

The dynamical regime associated with the Earth–Moon–Sun system is rich with complexity and includes intricate perturbations that lead to chaotic behavior. After characterizing an orbit, one that is slightly perturbed from and generally resembling the TESS DRM, this analysis further examines modes of evolving trajectory behavior in the nearby phase space. It is observed that contributing factors leading to transitioning behavior in associated long-term solutions are coupled and cumulative. Moreover, the sensitive nature of the design space generally overshadows any independent contribution. Transitions are likely associated with energy shifts over time that increase the chaoticity of the system. In the resulting, more complex environment, long-term increased stability options become available, but

it is observed that the increased sensitivity of the system can potentially perturb results in an unfavorable way. Care is warranted if such increased-stability options are considered for mission applications.

Acknowledgements The authors wish to acknowledge Dr. Natasha Bosanac, Dr. Loïc Chappaz, Dr. Davide Guzzetti and Dr. Diogo Sanchez for special insight and assistance with the various approaches for this analysis. This work is supported in part by the Rune and Barbara Eliasen Aerospace Visualization Laboratory at Purdue University. The facilities of the Eliasen Lab have been leveraged heavily for computation and the production of visuals for this paper. Additional support for this effort from the Purdue University School of Aeronautics and Astronautics and College of Engineering is also acknowledged and appreciated.

References

Anderson, R.L., and Lo, M.W.: Role of Invariant Manifolds in Low-thrust Trajectory Design. J. Guid. Control Dynam., **32(6)**, 1921–1930 (2009)

Anderson, R.L., Lo, M.W., and Born, G.H.: Application of Local Lyapunov Exponents to Maneuver Design and Navigation in the Three-Body Problem. In: AAS/AIAA ASC, Big Sky, Montana (2003)

Blazevski, D., and Ocampo, C.: Periodic orbits in the concentric circular restricted four-body problem and their invariant manifolds. Physica D, **241**, 1158–1167 (2012)

Bosanac, N., Howell, K.C., and Fischbach, E.: Exploring the Impact of a Three-Body Interaction Added to the Gravitational Potential Function in the Restricted Three-Body Problem. In: AAS/AIAA SFM Meeting, Kauai, Hawaii (2013)

Carrico Jr., J., Dichmann, D., Policastri, L., Carrico III, J., Craychee, T., Ferreira, J., Intelisano, M., Lebois, R., Loucks, M., Schrift, T., and Sherman, R.: Lunar-Resonant Trajectory Design for the Interstellar Boundary Explorer (IBEX) Extended Mission. In: AAS/AIAA ASC, Girdwood, Alaska (2011)

Colombo, C.: Long-term Evolution of Highly-Elliptical Orbits: Luni-solar Perturbation Effects for Stability and Re-entry. In: AAS/AIAA SFM Meeting, Williamsburg, Virginia (2015)

Colombo, C., Alessi, E.M., van der Weg, W., Soldini, S., Letizia, F., Vetrisano, M., Vasile, M., Rossi, A., and Landgraf, M.: End-of-life disposal concepts for Libration Point Orbit and Highly Elliptical Orbit missions. Acta Astron., **110**, 208–312 (2015)

Diacu, F.: The Solution of the n-body Problem. Math. Intell., **18(3)**, 66–70 (1996)

Dichmann, D.J., Parker, J.J.K., Williams, T., and Mendelsohn, C.R.: Trajectory Design for the Transiting Exoplanet Survey Satellite. In: ISSFD, Laurel, Maryland (2014)

Dichmann, D.J., Lebois, R., and Carrico, J.P.: Dynamics of Orbits Near 3:1 Resonance in the Earth–Moon System. J. Astronaut. Sci., **60(1)**, 51–86 (2015)

Dichmann, D., Parker, J., Nickel, C., and Lutz, S.: Trajectory Design Enhancements to Mitigate Risk for the Transiting Exoplanet Survey Satellite (TESS). In: AIAA Space, Long Beach, California (2016)

Farazmand, M., and Haller, G.: Computing Lagrangian coherent structures from variational LCS theory. Chaos, **22**, 013128-1–12 (2012)

Gangestad, J.W., Henning, G.A., Persinger, R., and Ricker, G.R.: A High Earth, Lunar Resonant Orbit for Lower Cost Space Science Missions. In: AAS/AIAA ASC, Hilton Head, South Carolina (2013)

Guzman, J.: Spacecraft Trajectory Design in the Context of a Coherent Restricted Four-Body Problem. Ph.D. Dissertation, Purdue University, West Lafayette, Indiana (2001)

Haller, G.: Distinguished material surfaces and coherent structures in three-dimensional fluid flows. Physica D, **149**, 248–277 (2001)

Harden, G.K., Haapala, A.F., Howell, K.C., and Marchand, B.G.: Automated Patch Point Placement for Spacecraft Trajectory Targeting. In: AAS/AIAA SFM Meeting, Santa Fe, New Mexico (2014)

Harris, F.J.: On the use of windows for harmonic analysis with the discrete Fourier transform. Proc. IEEE, **66(1)**, 51–83 (1978)

Howell, K.C., and Davis, D.C.: Spacecraft Trajectory Design Strategies Based on Close Encounters with a Smaller Primary in a 4-body Model. In: AAS/AIAA ASC, Honolulu, Hawaii (2008)

Koon, W.S., Lo, M.W., Marsden, J.E., and Ross, S.D.: Constructing a Low Energy Transfer Between Jovian Moons. Contemp. Math., **292**, 129–145 (2002)
Kozai, Y.: Secular perturbations of asteroids with high inclinations and high eccentricity. Astron. J., **67**, 591–598 (1962)
Lidov, M.: The Evolution of Orbits of Artificial Satellites of Planets under the Action of Gravitational Perturbations of External Bodies. Planet. Space Sci., **9**, 719–759 (1962)
Parker, J.S., and Lo, M.W.: Unstable Resonant Orbits Near Earth and Their Applications in Planetary Missions. In: AIAA GNC Conference, Providence, Rhode Island (2004)
Pavlak, T.A., and Howell, K.C.: Evolution of the Out-of-Plane Amplitude for Quasi-Periodic Trajectories in the Earth–Moon System. Acta Astron., **81(2)**, 456–465 (2012)
Prado, A.F.B.A.: Searching for Orbits with Minimum Fuel Consumption for Station-Keeping Maneuvers: An Application to Lunisolar Perturbations. Mathematical Problems in Engineering, **2013**, 415015-1–11 (2013)
Prado, A.F.B.A.: Mapping orbits around the asteroid $2001SN_{263}$. Advances in Space Research, **53**, 877–889 (2014)
Sanchez, D.M.: On the effects of each term of the geopotential perturbation along the time I: Quasi-circular orbits. Advances in Space Research, **54**, 1008–1018 (2014)
Short, C.R., and Howell, K.C.: Lagrangian coherent structures in various map representations for application to multi-body gravitational regimes. Acta Astron., **94(2)**, 592–607 (2014)
Short, C.R., Blazevski, D., Howell, K.C., and Haller, G.: Stretching in Phase Space and Applications in General Nonautonomous Multi-body Problems. Celest. Mech. Dyn. Astron., **122(3)**, 213–238 (2015)
Smith, D.R.: An Introduction to Continuum Mechanics — after Truesdell and Noll. Kluwer, Dordrecht (1993)
Szebehely, V.: Theory of Orbits, the Restricted Problem of Three Bodies. Academic Press, New York (1967)
Vaquero, M., and Howell, K.: Leveraging Resonant Orbit Manifolds to Design Transfers between Libration Point Orbits. J. Guid. Control Dynam., **37(4)**, 1143–1157 (2014)